Contractor EU 7th Frame Programme

Subject Thermo-physical properties of TBCs and effects of simulated combusted syngas environments

Contract 239349

Notes Deliverable of the H2IGCC project D2.2.7

N. of pages 43 **N. of pages annexed** 0

Issue date 30/11/2012

Prepared SSG - S. Capelli, F. Cernuschi, L. Lorenzoni
with the contribution of P. Bison and A. Bortolin of CNR-ITC

Approved SSG – L. Mazzocchi

Ricerca sul Sistema Energetico – RSE S.p.A.
Società con unico socio soggetta alla direzione ed al coordinamento di GSE S.p.A.
Sede Legale - 20134 Milano - Via R. Rubattino, 54
Tel. +39 023992.1 - Fax +39 023992.5370 - PEC rse@legalmail.it
Reg. Imprese di Milano, P.IVA e C.F. 05058230961
R.E.A. di Milano n. 1793295
Cap. Soc. € 1.100.000 i.v.

Table of contents

REVISIONS HISTORY

Revision number	Date	Protocol	List of modifications and/or modified paragraphs
0	30/11/2012	12005237	First emission

1 FOREWORD

The overall objective of the H2-IGCC project is to provide and demonstrate technical solutions which will allow the use of state-of-the-art highly efficient, reliable gas turbines (GTs) in the next generation of Integrated Gasification Combined Cycle (IGCC) plants. The goal is to enable combustion of undiluted hydrogen-rich syngas with low NOx emissions and also allowing for high fuel flexibility. The challenge is to operate a stable and controllable GT on hydrogen-rich syngas with emissions and processes similar to current state-of-the-art natural GT engines. The H2-IGCC project aims to tackle this challenge as well as fuel flexibility, by enabling the burning of back-up fuels, such as natural gas, without adversely affecting the reliability and availability.
The technical challenges being addressed by the H2-IGCC project are divided into 4 Subprojects (SP):

- COMBUSTION (SP1)
- MATERIALS (SP2)
- TURBOMACHINERY (SP3)
- SYSTEM ANALYSIS (SP4)

In particular, SP2 deals with improved materials systems with advanced coatings able to protect hot path components base materials against different temperatures and compositions of exhaust gases. Cost-effective materials and coatings technologies will be developed to overcome the component life-limiting problems of overheating and of hot corrosion resulting from the higher temperatures and residual contaminants in the syngas, including validation of materials performance data, life prediction and monitoring methods. Simulation tools for estimating performance and lifetime of materials systems will also be enhanced to suit the new operating environments.

This report summarises the activities aimed to study the thermo-physical properties of TBCs and the effects of simulated combusted syngas environment.
In particular, thermal diffusivity have been measured on samples in as sprayed conditions and after aging at high temperatures in air and in an environment simulating the combustion gases of a GT fuelled by a hydrogen rich syngas.
Furthermore, thermal diffusivity has been measured in different conditions (i.e. having different gases at different pressures inside the TBC pores, as better explained later) for studying the microstructural evolution of TBC as a function of aging.

2 EXPERIMENTAL MATRIX

Thermal diffusivity has been measured by using the Laser flash technique on samples in the as – sprayed condition and after aging.

Thermal diffusivity measurements have been carried out on 10 mm diameter specimens machined from the supplied TBCs. In fact, since thermal diffusivity measurements by laser flash technique have to be carried out preferable on freestanding samples, TBC have been deposited onto graphite plates to rend easier the TBC removal by partially burning the substrate in furnace at 650°C.

Measurements have been carried out in agreement with ASTM 1461-01 at Room Temperature (RT), 400°C, 800°C, 1000°C, 1050°C, 1100°C, 1150°C, 1200°C and 1250°C. At RT, measurements have been carried out in different gases (He, Ar and N_2) at different pressures (0.9 bar, 0.75 bar 0.25 bar and 0.05 bar) and in vacuum. At high temperatures, measurements have been carried out in vacuum.

Taking into account the following relationship among thermal diffusivity α and thermal conductivity k:

$$\alpha = k/\rho\, C_p$$

thermal conductivity k has been estimated by using literature values of YPSZ for theoretical density and thermal expansion coefficient at the measurement temperatures. In particular, for each sample, RT density ρ has been estimated from the theoretical value of YPSZ by measuring the porosity content by IA on 5 Back Scattered Images (BEI) of the cross section after vacuum impregnation by epoxy resin. To estimate the high temperature values of the density, literature value for the coefficient of thermal expansion (CTE) in the temperature range chosen for thermal conductivity evaluation, have been considered. CTE is also used for correcting the sample thickness at high temperature in the thermal diffusivity estimation procedure.

The specific heat *Cp* has been measured for the different aging conditions by the differential scanning calorimetry.

Results of thermal diffusivity measured at RT by Laser Flash technique have been compared with those obtained on samples tested in the frame of the WP 2.3 (Advanced NDE and monitoring methods) by using a thermographic technique described in details later within the report.

3 THERMAL DIFFUSIVITY MEASURING TECHNIQUES

The most worldwide applied technique for the measurement of the thermal diffusivity of solid materials is the laser flash method [1, 2]. More specifically, this method consists in heating the front face of a sample (typically a small disk shape specimen) by a short laser pulse and in detecting the temperature rise on its rear surface. The main advantages of this method are the simplicity, the rapidity and the possibility to measure the thermal diffusivity on a wide range of materials also within a wide temperature range. Recently a thermographic technique suitable to be applied without requiring a specific sample preparation has been developed.

3.1 Laser Flash

3.1.1 Theoretical remarks

The mathematical model utilized to describe the heat conduction problem that arises in the Laser Flash experiment is the following (see Figure 1):

- a slab of thickness L
- heat flux prescribed on one side (z=0) of the slab, consisting of a pulse of finite duration t_h
- heat exchange with the environment according to the linear Newton law on the heated side, adiabatic on the back side (z=L) where temperature is measured.

The solution for the temperature T on the back side of the slab(z=L) is given by:

$$T(t)=\frac{Q}{h}\sum_{i=1}^{\infty}\frac{2\sin\mu_i}{\mu_i+\sin\mu_i\cos\mu_i}\left[\exp\left(-\mu_i^2\frac{\alpha}{L^2}(t-t_h)\right)-\exp\left(-\mu_i^2\frac{\alpha}{L^2}t\right)\right] \quad (1)$$

- Q power of the pulse during the heating time [Wm^{-2}]
- h heat exchange coefficient [$Wm^{-2}K^{-1}$]
- α thermal diffusivity [m^2s^{-1}]
- L specimen thickness [m]
- t time [s]
- t_h pulse duration [s]
- μ_i i_{th} positive root of the transcendental equation (attenzione alla definizione di Biot che era sbagliata nella versione che ti ho mandato) $\mu_i\tan\mu_i = Bi$ $\quad Bi = {hL}/{\lambda}$
- λ thermal conductivity [$Wm^{-1}K^{-1}$]

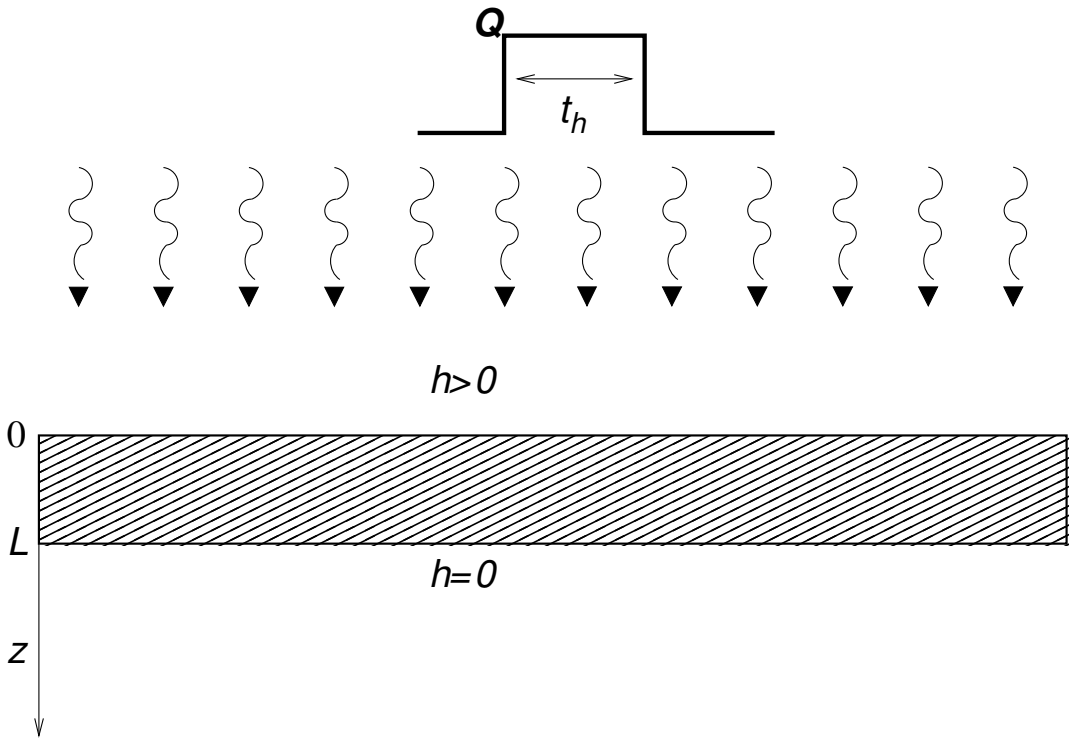

Figure 1. Scheme of the mathematical model that describes the Laser Flash experiment.

In the most simple case without heat losses and a Dirac (i.e. instantaneous) energy pulse Eq.(1) simplifies as [1]:

$$V(t) = \frac{T(L,t)}{T_\infty} = 1 + 2\sum_{n=1}^{\infty}(-1)^n \exp(-n^2\pi^2 t / t_c) \qquad (1)$$

where, $T_\infty = \frac{Q}{\rho C L}$ and $t_c = \frac{L^2}{\alpha}$ are the heating pulse intensity, the equilibrium temperature and characteristic time, respectively. The graphical representation of Eq.(1) is shown in Figure 2.

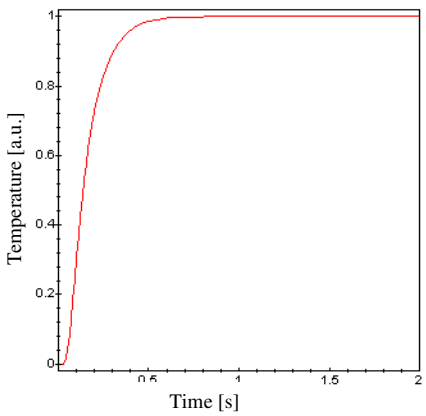

Figure 2 V(t) vs. the time.

The evaluation of the thermal diffusivity from the experimental data can be obtained considering the following relation [1,2]:

$$\alpha = 0.13885 \frac{L^2}{t_{1/2}} \tag{2}$$

where $t_{1/2}$ is the time corresponding to the half maximum increase of V(t). Similar relationships can be obtained for times $t_{x\%}$ corresponding to different percentages $x\%$ of the maximum temperature increase [3]. Nowadays, thermal diffusivity is often estimated by fitting the whole experimental data using eq.(1). When radiative heat losses cannot be neglected, several different data correction can be applied. In the frame of this work the following corrections have been applied and the average value of the corrected thermal diffusivity has been reported.

The Cowan method (cooling curve correction)

The Cowan method requires to determine the ratio of the net rise-time temperature values at times which are five or ten times the experimental half-time temperature values, to the net rise at the half-time temperature value (see Figure 3). These two ratios are named Δt_5 and Δt_{10}, respectively. The correction factor K_c for five and ten half-time cases can be obtained from the polynomial fits [4]:

$$K_C = A + B(\Delta t) + C(\Delta t)^2 + D(\Delta t)^3 + E(\Delta t)^4 + F(\Delta t)^5 + G(\Delta t)^6 + H(\Delta t)^7 \tag{3}$$

where Δt in Eq.(3) refers to Δt_5 or Δt_{10}, respectively.

Thus the corrected value of the thermal diffusivity can be obtained as [4]:

$$\alpha_{corrected} = \alpha \; K_C \; / \; 0.13885 \tag{4}$$

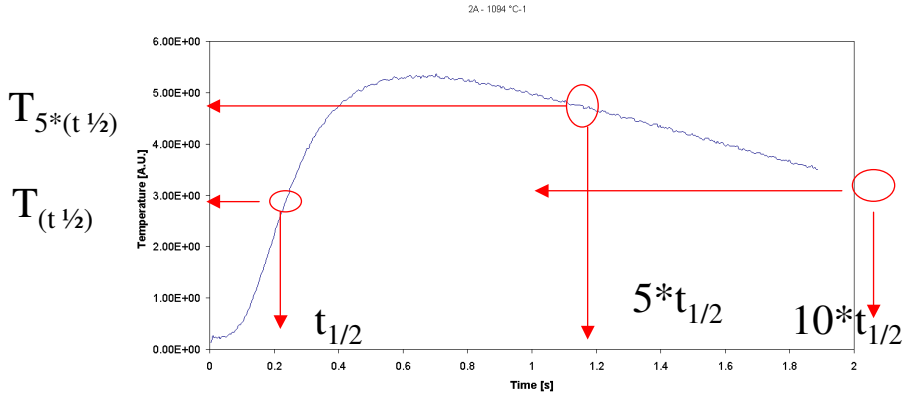

Figure 3. Sketch of the experimental points used for correcting the thermal diffusivity value.

The ratio method (rise curve correction)

The heat loss correction on the rise curve data also employ the ratio technique. For the ratio $t_{0.75}/t_{0.25}$ (where times $t_{0.75}$ *and* $t_{0.25}$ refer to the times corresponding to the 0.75 and 0.25 of the maximum temperature increase) the ideal value is 2.272. this ratio must be determined from the experimental data. Then the correction factor K_R can be calculated from the equation:

$$K_R = -0.3461467 + 0.361578(t_{0.75}/t_{0.25}) - 0.06520543(t_{0.75}/t_{0.25})^2 \quad (5)$$

The corrected value $\alpha_{corrected}$ of thermal diffusivity at half-time $\alpha_{0.5}$ is:

$$\alpha_{corrected} = {}^{\alpha_{0.5}K_R}/_{0.13885} \quad (6)$$

The corrections using many other ratios is suggested.

Non-linear data fitting

The model of eq. 1 depends on some known data and some unknown parameters. The known data are the times *t* of temperature acquisition, that are determined by the sampling rate of the acquisition board, and the pulse duration t_h that is a setting parameter of the laser equipment.
The unknown parameters are the set:

$$P=\{p_1, p_2, p_3\}=\left\{\frac{Q}{h}, \frac{\alpha}{L^2}, Bi\right\} \quad (7)$$

The fitting procedure changes iteratively the parameters P trying to minimize the difference between data and model according to the mean least square criterion. Once a minimum is reached, the obtained parameters can be considered the best set that approximates the *true* values and in particular the p_2 parameter furnishes the diffusivity, once the thickness of the sample is known.

3.1.2 Experimental set-up

The experimental system (Theta Industries Inc., Port Washington, NY, USA) shown in Figure 4 uses a pulsed (500µs) 1.064µm wavelength Nd:YAG laser for heating the sample. The pulse energy can be tuned in the range 0.5-21 J. The beam shape is circular with an almost uniform intensity 12 mm diameter. Samples are allocated within a furnace where it is possible to reach 1400°C. The sample and the furnace are both inside a chamber where the gas and pressure can be set up. An infrared detector monitors the temperature of the rear face of the sample through an infrared window. The signal is then amplified, acquired and elaborated by a PC.
Measurement on each sample consists in evaluating its thermal diffusivity at some of the following seven different temperatures in the range 20°C - 1250°C:

20°C, 400°C, 800°C, 1000°C, 1050°C, 1100°C, 1150°C, 1200°C and 1250°C.

To collect statistically meaningful data, measurements were repeated five times for each condition. Owing to the TBC translucency, prior to evaluating the thermal diffusivity, thin layers of colloidal graphite were painted on both sample surfaces, respectively to make the TBC front face opaque to the Nd:YAG laser radiation and to increase the rear face emissivity in the IR detector sensitivity range (3 – 5 µm). Typical rear face temperature increases as a function of time are shown in Figure 5.

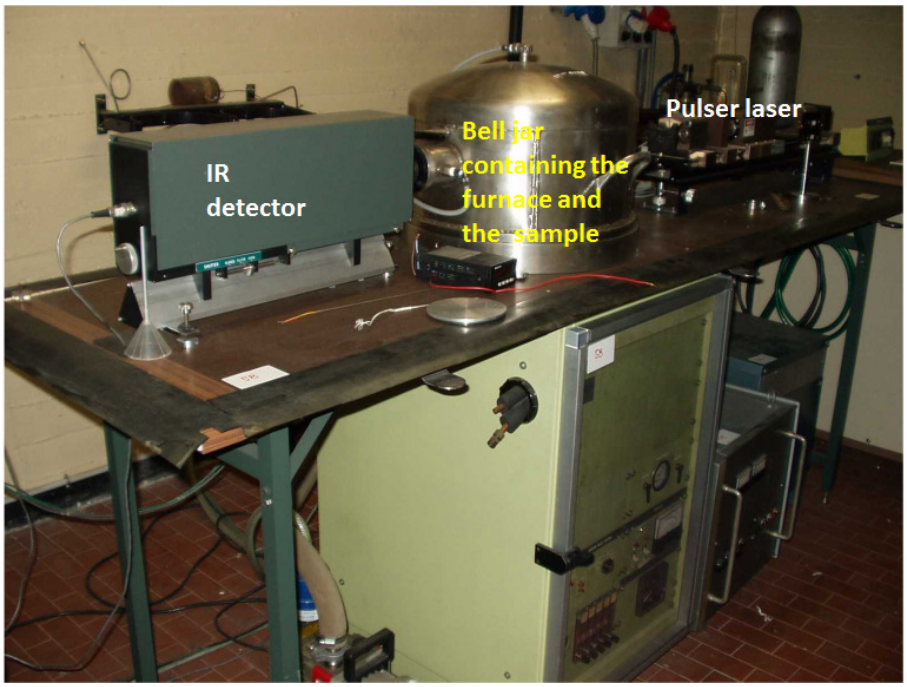

Figure 4. Overall view of the laser flash equipment.

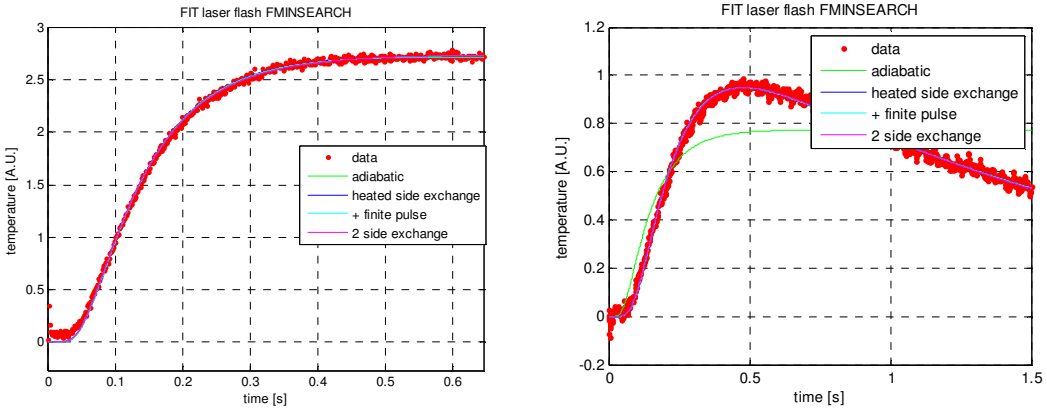

(a) (b)

Figure 5. Rear face temperature increase vs. time for sample R286-1. Measurements have been carried out (a) at RT in vacuum and no heat losses can be observed in the curve, (b) at 1250°C in vacuum. Observe the significant drop of the temperature due to radiative heat losses at high temperature.

3.2 Thermographic method

3.2.1 Theoretical remarks

To measure the thermal diffusivity of TBC deposited onto substrates without requiring a specific sample preparation, a one side transient thermal test was developed at RSE in collaboration with ITC-CNR.
The geometry of the thermal problem considers a plane layer (coating) on a semi-infinite substrate. The thermal conductivity of coating is assumed to be anisotropic and oriented according to the in-plane and through-the-thickness directions. The substrate is assumed thermally isotropic. No exchange with the environment is considered. For the sake of simplicity a circular symmetry of the heating source is assumed, hence the heating shape $f(r)$ does not depend on the angle in the coordinate system (r,θ). With such assumptions, the solution for the temperature on the surface is obtained as an extension of the formula for the slab by Philippi et al. [5, 6]. It is expressed in terms of the spatial Fourier-Bessel transform of the surface temperature as a function of time:

$$\Theta_c\left(k, z=0, t\right) = F(k) e^{-\alpha_P k^2 t} L^{-1}\left[\frac{1}{\lambda_N q_N}\left[\frac{1+\Gamma_{3D} e^{-2q_N l_c}}{1-\Gamma_{3D} e^{-2q_N l_c}}\right]\right] \qquad \Gamma_{3D} = \frac{\varepsilon_c - \varepsilon_s\sqrt{1+\frac{\Delta\alpha}{\alpha_N}\frac{k^2}{q_N^2}}}{\varepsilon_c + \varepsilon_s\sqrt{1+\frac{\Delta\alpha}{\alpha_N}\frac{k^2}{q_N^2}}} \quad (8)$$

$$q_N = \sqrt{\frac{p}{\alpha_N}} \qquad \Delta\alpha = \alpha_S - \alpha_P$$

Here, $F(k)$ is the Fourier-Bessel Transform of the heating function $f(r)$, α_P and α_N are respectively the in-plane (parallel) and through-the-thickness (normal) diffusivities of coating, while α_S is that of substrate; λ_N is the normal conductivity of coating, while ε_C and ε_S are the effusivities of coating and substrate respectively. Finally, l_c is the coating thickness, p is the Laplace Transform variable while L^{-1} is the inverse Laplace transform that, on the lack of an explicit inversion, can be computed with any numerical algorithm (e.g. Stephest's [7]).
A particularization of Eq. (8) is obtained when the zero-frequency of the Fourier-Bessel variable is considered, viz. k=0. In such a case $\Gamma_{3D}\rightarrow\Gamma_{1D}= (\varepsilon_C-\varepsilon_S)/(\varepsilon_C+\varepsilon_S)$ and an explicit Laplace inversion is available for the expression indicated inside the L^{-1} sign. Moreover, taking the k=0 frequency in Eq. (8)

corresponds to integrate spatially the surface temperature. From the definition of the Fourier-Bessel Transform, where J_0 is the Bessel function of zero order one obtains:

$$\Theta_C(k=0,z=0,t)=\frac{Q_0}{\varepsilon_C\sqrt{\pi t}}\left[1+2\sum_{n=1}^{\infty}\Gamma_{1D}\,e^{-\frac{n^2 l_c^2}{\alpha_N t}}\right]=\frac{1}{2\pi}\int_0^{2\pi}d\theta\int_0^{\infty}rJ_0(0)T_C(r,z=0,t)dr=\frac{1}{2\pi}\int_{-\infty}^{\infty}\int_{-\infty}^{\infty}T_C(x,y,z=0,t)dxdy \tag{9}$$

where $T(x,y,z=0,t)$ is the surface temperature field, t is time, Q_0 the total energy released by the pulse, and Γ_{1D} is the so called mismatch coefficient between coating and substrate. Notice that eq. (9) corresponds to the solution that one obtains in case a spatially uniform pulse (instead of a localized one) heats the surface of our system, provided that Q_0 be interpreted as the specific energy.
In conclusion, using Eq. (8) one fits the spatial Fourier transform of a thermographic sequence to estimate the in-plane diffusivity; using Eq. (9) one fits the spatial integral of the thermographic sequence to estimate the through-the-thickness diffusivity. In the following, Eq. (9) will be applied to estimate the through-the-plane thermal diffusivity of TBCs.

3.2.2 The experimental set-up

A Nd:YAG laser (1064 nm wavelength) generating a pulses of about 0.5 ms was used as heating source. The energy and the diameter of the heating pulse were fixed roughly equal to 0.5 J and 10 mm, respectively.
An IR CEDIP camera Jade II sensitive within the spectral range 7 – 10 µm grabbed the sequence of thermograms of the specimen surface at a frame rate of 140 Hz (see Figure 6 for the experimental set-up) for 3 seconds. For each sample, thermal diffusivity measurements have been carried out at least five times to have some statistics.

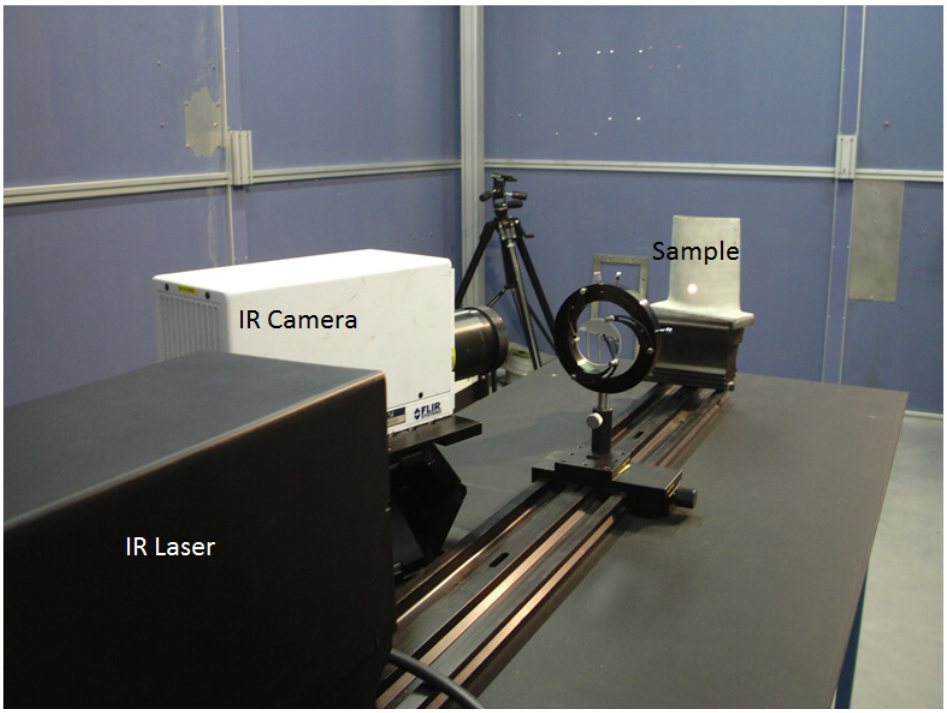

Figure 6. Experimental set-up. A pulsed laser shots the TBC specimen. The IR camera grabs a sequence of images of the specimen surface temperature.

Figure 7 shows, in a bi-logarithmic scale, the time evolution of the surface temperature after the laser shot, together with the interpolating function that fits the data and the value of the estimated α/L^2 parameter. Data are relative to the spatial average temperature in a suitable area containing the entire detectable signal. A non linear best fit procedure is used to obtain the parameter of interest based on the minimization of the sum of the squared differences between the data and the model of Eq. (9).

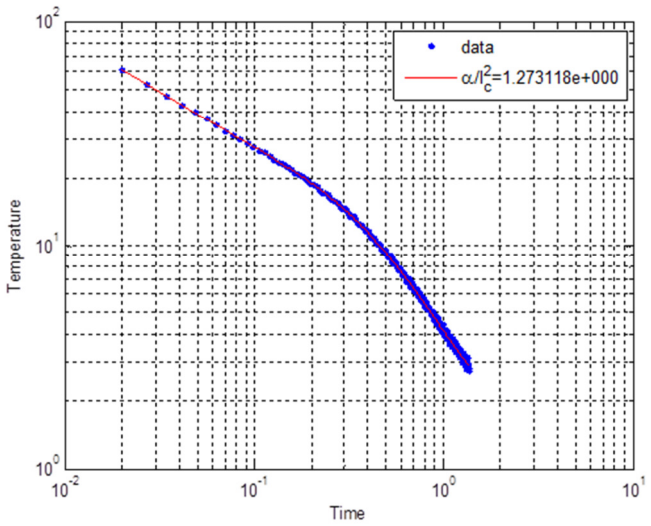

Figure 7. Temperature vs. time experimental data and fitting curve in bi-logarithmic scale.

4 SPECIFIC HEAT MEASUREMENTS

4.1 Theoretical remarks

Differential scanning calorimetry (DSC) is a simple and fast technique for determining the specific heat of material in a wide temperature range. DSC allows also to detect heat effects associated with phase transitions and chemical reactions as a function of temperature. During a DSC experiment the signal coming from the sample is monitored and compared to that of a reference sample when a linear cooling/heating ramp is applied.
There are mainly two different types of DSC experiments depending on the signal monitored during the experiment:

- The difference between the power that has to be supplied to the sample and the reference, respectively to guarantee that both have the same temperature ramp.
- The temperature difference between the sample and an empty crucible when there is a single heating/cooling source (typically a furnace).

Independently from the experimental configuration to estimate the specific heat the signal S consists of two contributions:

$$S=I+K(T, v)\Delta C(T) \tag{10}$$

where $I(T)$ is the isothermal signal caused by the heat transfer among the two measurement channels and the surrounding. The second term is the contribution arising from the difference of the thermal capacity of the two measurement positions:

$$K\Delta C=K(\Delta C_e+m_xC_{px}) \tag{11}$$

where ΔC_e, m_x e C_{px} are the difference of thermal capacities of the two empty measurement channels, the mass and the specific heat of the sample present in the measurement channel, respectively (x can be equal to s (sample) or r (reference). K is a constant which depends not only on the temperature but even on the heating/cooling rate v.

Usually three measurements are carried out in a sequence:

i. Both channels empty:

$$S_e=I+ K\Delta C_e \tag{12}$$

ii. Reference sample in the measurement channel:

$$S_r=I+ K(\Delta C_e+ m_rC_{pr}) \tag{13}$$

iii. Sample whose C_{ps} has to be measured in the measurement channel:

$$S_s=I+ K(\Delta C_e+ m_sC_{ps}) \tag{14}$$

By subtracting Eq.(12) from Eq. (13) and Eq. (14) and considering the ratio:

$$C_{ps} = \frac{S_s - S_e}{S_r - S_e}\frac{m_r}{m_s}C_{pr} \tag{15}$$

Although the performances of state-of-the-art instruments guarantee experimental uncertainty within ±1 – 2% the use of not properly prepared samples and wrong calibrations can become sources of significantly higher uncertainty.

4.2 The experimental set up

The specific heat measurements of TBC were performed by two Differential Scanning Calorimeters (DSC): SETARAM DSC 111 and Netzsch DSC 404.
The experimental configuration adopted by both instruments gives the signal of the temperature difference between the two channels surrounded by a furnace. On as sprayed samples two different scanning rates were chosen (4K/min and 10 K/min) in the temperature range of 60 °C up to 850°C and 1250°C to assess the independence of specific heat values from the heating rate. Measurements were carried out in air atmosphere using alumina crucibles.

5 EXPERIMENTAL

5.1 The samples

The state of the art TBC coatings selected in the frame of this project are:

- standard porous (SP) air plasma spray (APS) TBC made of Yttria Partially Stabilised (7 – 8%wt.) Zirconia (YPSZ). These samples have been sprayed on a graphite plate to allow the TBC removal without using any chemical etching of the metallic substrate. In fact in this case it is just sufficient to put the coated plate in a furnace at 650°C for few hours to partially burn the graphite.
- Dense highly vertically cracked (VC) YPSZ TBC deposited by APS.

Table 1and Table 2 resume the codes and features of the samples considered in the frame of this activity and in the WP2.3 (but included also in this WP for comparison purposes), respectively.

The Table 3 resumes the codes and the main features of the samples considered for the specific heat measurements.

Table 1 The samples used for thermal diffusivity measurements

Sample code	TBC type	Aging temperature [°C]	Aging time [h]	Aging environment	Aging continuous/ cyclic	Measurement technique
R286-1	SP/F	As sprayed	0	n.a	n.a	L.F.
R286-5	SP/F	As sprayed	0	n.a	n.a	L.F
R287-1	SP/F	1000	500	Air+20% H2O	Continuous	L.F
R287-5	SP/F	1100	500	Air+20% H2O	Continuous	L.F
R287-9	SP/F	1200	500	Air+20% H2O	Continuous	L.F
R287-10	SP/F	1250	500	Air+20% H2O	Continuous	L.F
R251-2	VC/F	As sprayed	0	n.a	n.a	L.F
R267-6	VC/F	1200	500	Air+20% H2O	Continuous	L.F
R267-7	VC/F	1250	500	Air+20% H2O	Continuous	L.F
R320-1	SP/F	1100	500	Air	Continuous	L.F.
R320-6	SP/F	1200	500	Air	Continuous	L.F.

Table 2 The samples aged in the frame of WP2.3. but considered also in this WP for comparison purposes

Sample code	TBC type	Aging temperature [°C]	Aging time [h]	Aging environment	Aging continuous/cyclic	Measurement technique
R245-2	SP/F	1080	265.5	Air	Cyclic	Thermography
R245-5	SP/F	1080	265.5	Air	Cyclic	Thermography
R270-3	SP/F	1080	316.5	Air	Cyclic	Thermography
R270-6	SP/F	1080	228	Air	Cyclic	Thermography
R269-4	VC/F	1080	334.5	Air	Cyclic	Thermography

Table 3 The samples used for the Specific heat measurements

Sample code	TBC type	Aging temperature [°C]	Aging time [h]	Aging environment	Aging continuous/ cyclic
R286-1b	SP/F	As sprayed	0	n.a	n.a
R287-2	SP/F	1000	500	Air+20% H2O	Continuous
R287-4	SP/F	1100	500	Air+20% H2O	Continuous
R287-12	SP/F	1250	500	Air+20% H2O	Continuous

5.2 Microstructural characterisation of the state-of-the-art TBCs

To estimate the thermal diffusivity of the TBC, the thickness of each sample need to be measured as much accurately as possible[1]. Measuring the thickness analysing images taken along the sample section by optical or scanning electron microscopy is the best way of proceeding. Furthermore, since most of the times, thermal diffusivity changes vs. aging time and temperature are related with the microstructure evolution, microstructural characterisation by image analysis (IA) has been carried out on all the samples whose thermal diffusivity was measured. Limited to as sprayed samples, Mercury Intrusion Porosimetry (MIP) has been performed by FZJ on two similar free standing standard porous TBC samples for comparison purposes.

5.2.1 Image analysis

The microstructural characterisation of each sample listed in Table 1 has been performed by scanning electron microscopy (SEM) (MIRA XMH, Tescan, Brno, CK). The microstructure of both the upper surface and a fracture surface were observed by microscopy. After that, TBC specimens were impregnated in vacuum using epoxy resin to better discriminate between true pores and possible artefacts induced by cross-sectioning and polishing. Regarding the overall porosity evaluation, ten 700x back-scattered electron images (BEI) taken along each sample cross-section were considered for the image analysis (IA) (Screen Measurement, Laboratory Imaging Ltd., Praha, CZ). Sample thickness has been evaluated averaging 40 measurements taken all along the section.

The typical APS TBC microstructure consists in vertical intra-lamellar cracks (vertical cracks), horizontal inter-lamellar pores (horizontal pores) and globular voids. Although some of these pores incline in respect with the coatings orientation, generally these three families of pores are considered to be sufficient to describe TBCs microstructure.

To roughly estimate the percentages of these three families of pores all the pores have been classified depending on their elongation *e* (defined as the ratio between the maximum and the minimum Feret diameters of the object) and orientation in respect to the sample thickness.

[1] Since the fitting parameter is the ratio between the thermal diffusivity and the square of the sample thickness the experimental uncertainty is mainly related to the uncertainty in measuring the TBC thickness (x% in thickness uncertainty corresponds to 2x% in thermal diffusivity estimation)

In particular, as explained in details elsewhere, all pores having an elongation $e<2$ have been considered as "spherical" while those with $e>2$ have been considered lamellar shaped [8]. In fact, since horizontal pores and vertical cracks can hardly be considered as linear objects, their measured elongation is much shorter than the true ratio between length and width. Moreover, thin lamellar pores in binary images often appear as many separated smaller pores with the elongation smaller than that of the original single lamellar pore. For this reason, the elongation value of 2 has been assumed as the threshold between spherical and lamellar shaped pores. Eventually, orientations have been considered within 30° around the chosen direction. By this way, for each sample more than 65000 objects were classified in the horizontal pores, vertical cracks and globular voids, respectively.

Table 4 resumes the main outcomes of this characterisation for all the investigated samples.

Table 4 Main outcomes of the microstructural characterisation of TBC samples

Sample code	TBC type	Aging T [°C]	Aging Env.	Thickness [µm]	Overall porosity [%]	Lamellar horizontal pores [%]	Vertical cracks [%]	Lamellar pores elsewhere oriented [%]	Globular voids [%]
R286-1	SP/F	As sprayed	n.a	496±5	31.4±0.6	3.5	1.4	3.7	22.8
R286-5	SP/F	As sprayed	n.a	490±5	28.2±0.6	4.9	0.6	2.1	20.6
R287-1	SP/F	1000	Air+20% H2O	522±4	27.7±0.9	6.6	0.9	3.4	16.7
R287-5	SP/F	1100	Air+20% H2O	470±5	21.7±0.6	3.4	0.7	2.8	14.8
R287-9	SP/F	1200	Air+20% H2O	523±5	25.5±0.9	1.7	0.5	3.1	20.1
R287-10	SP/F	1250	Air+20% H2O	480±5	21.2±1	3.4	0.9	3	13.9
R251-2	VC/F	As sprayed	n.a	433±6	4.1±0.3	0.7	0.5	0.8	2.1
R267-6	VC/F	1200	Air+20% H2O	486±3	2.9±0.1	0.6	0.3	0.6	1.4
R267-7	VC/F	1250	Air+20% H2O	458±3	3.4±0.2	0.6	0.5	0.7	1.6
R320-1	SP/F	1100	Air	455±4	22.5±0.7	2.1	0.5	3.5	16.4
R320-6	SP/F	1200	Air	464±5	24.2±0.5	3.9	0.4	3.2	16.7
R245-1	SP	As sprayed	n.a	624±7	21.0±0.8	3.5	0.8	3.4	13.2

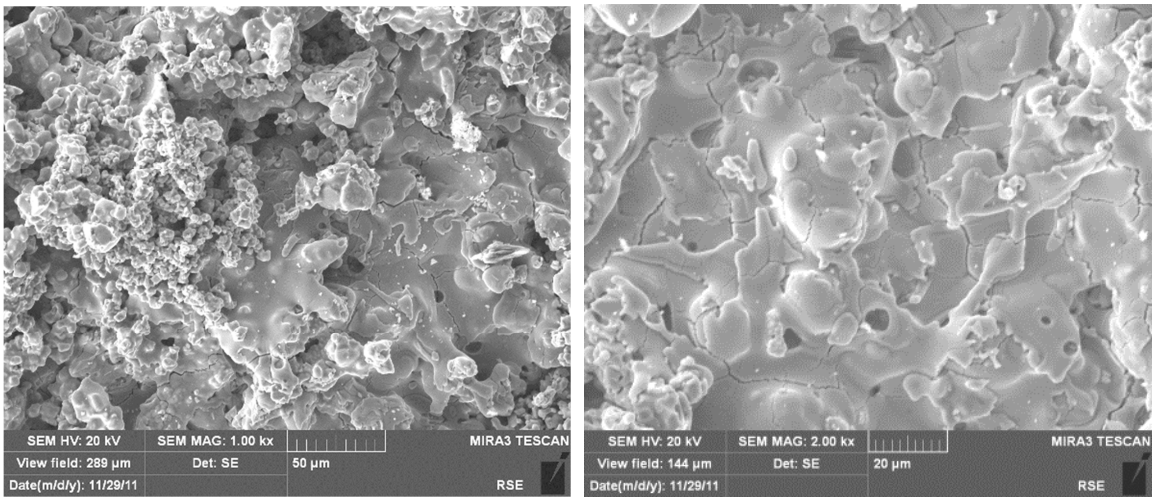

(a) **(b)**

Figure 8. Images at two different magnifications of the upper surface of the porous TBC. The network of vertical cracks can be clearly distinguished as well as the solidified splats. A fine porous structure is visible on the left of figure (a).

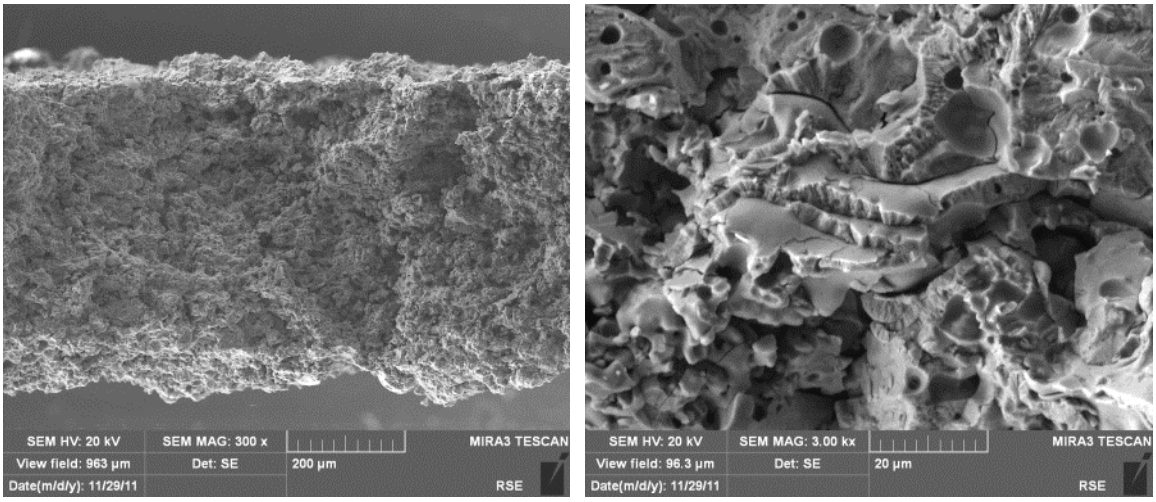

(a) **(b)**

Figure 9. Images at two different magnifications of the fracture surface of the porous TBC. The inter lamellar porosity oriented parallel to the external surface, the intra lamellar network of vertical cracks and the globular voids can be distinguished especially at the highest magnification.

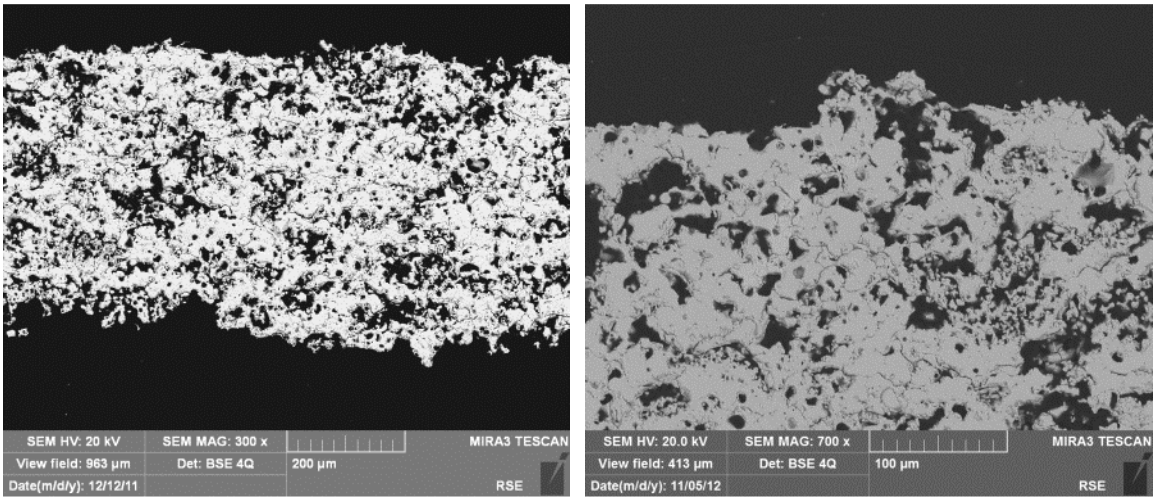

(a) **(b)**

Figure 10. Sample R286-1 (As sprayed). Images at two different magnifications of the section of the TBC. Inter-lamellar pores wide globular voids can be observed.

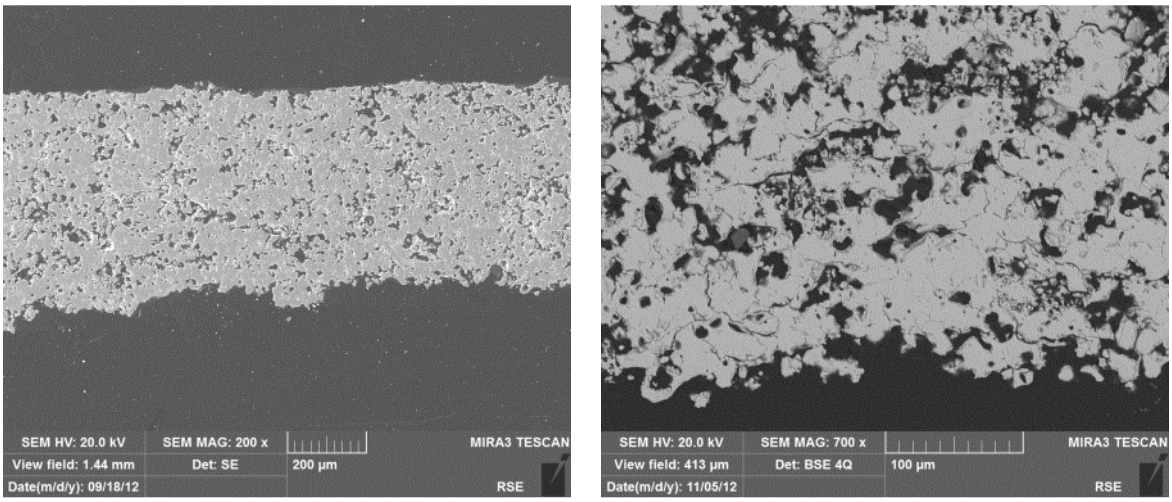

(a) **(b)**

Figure 11. Sample R287-1 (aged @1000°C for 500h) Images at two different magnifications of the section of the TBC.

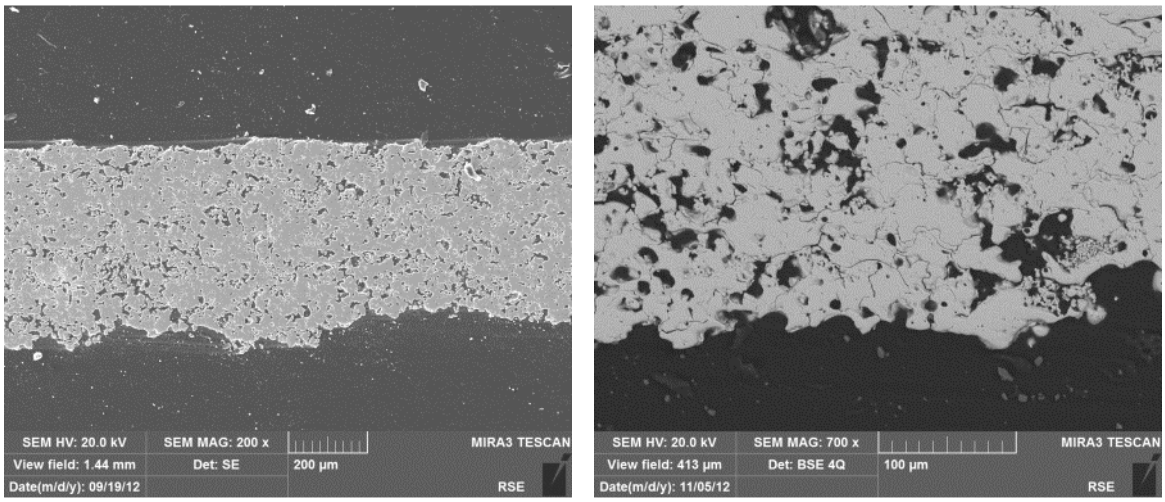

(a) **(b)**

Figure 12. Sample R287-5 (aged @1100°C for 500h) Images at two different magnifications of the section of the TBC.

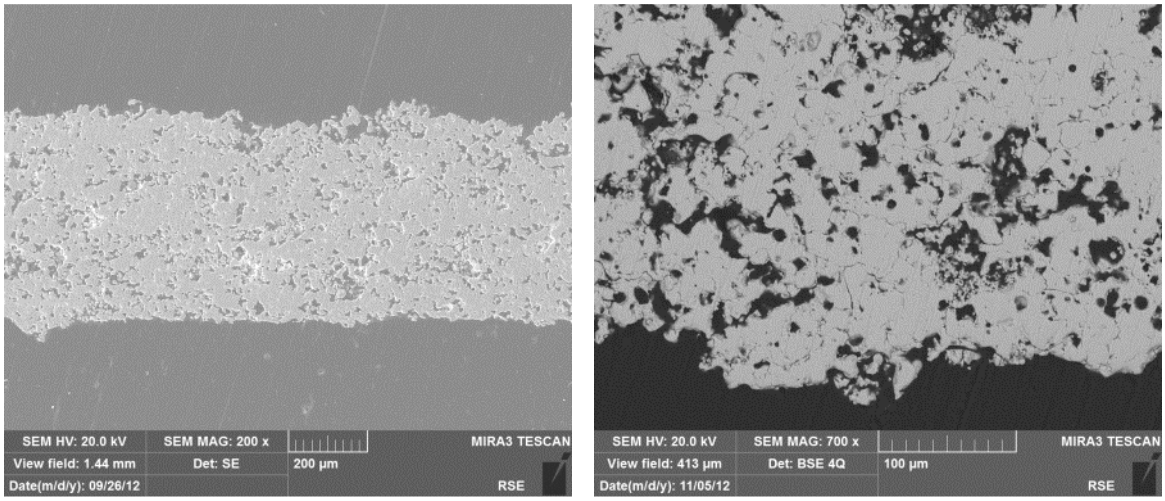

(a) (b)

Figure 13. Sample R287-9 (aged @1200°C for 500h) Images at two different magnifications of the section of the TBC.

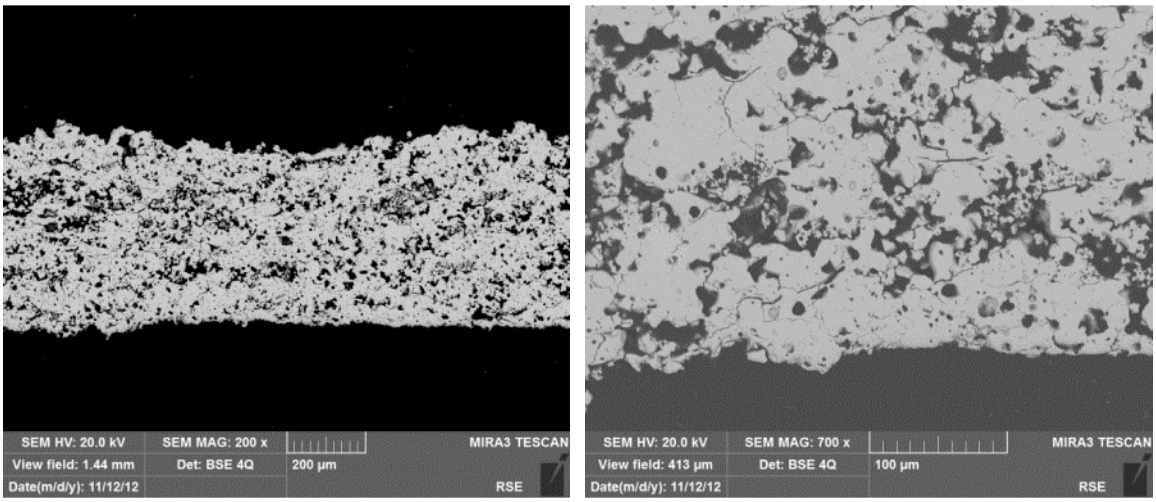

(a) (b)

Figure 14. Sample R287-10 (aged @1250°C for 500h) Images at two different magnifications of the section of the TBC.

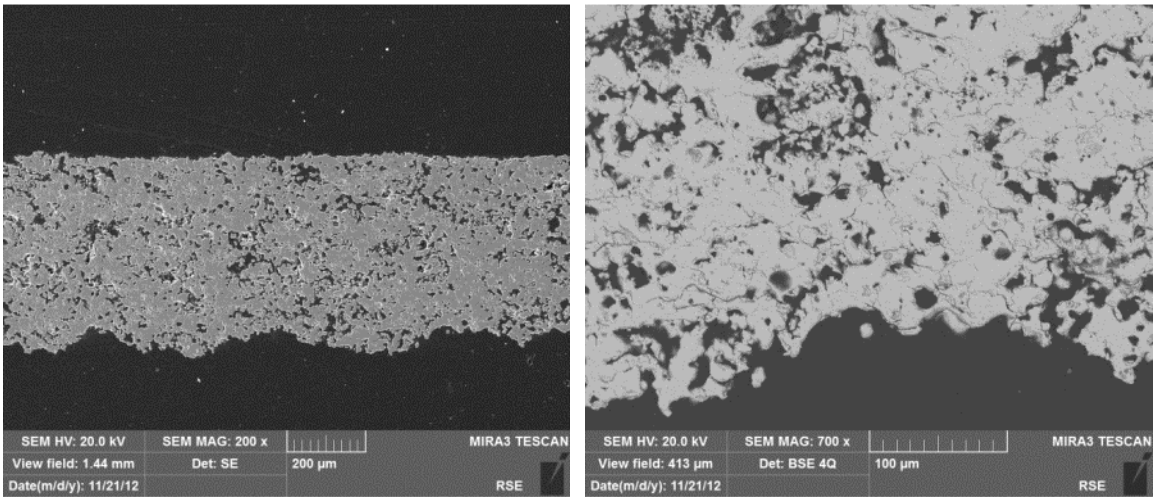

(a) (b)

Figure 15. Sample R320-1 (aged @1100°C for 500h) Images at two different magnifications of the section of the TBC.

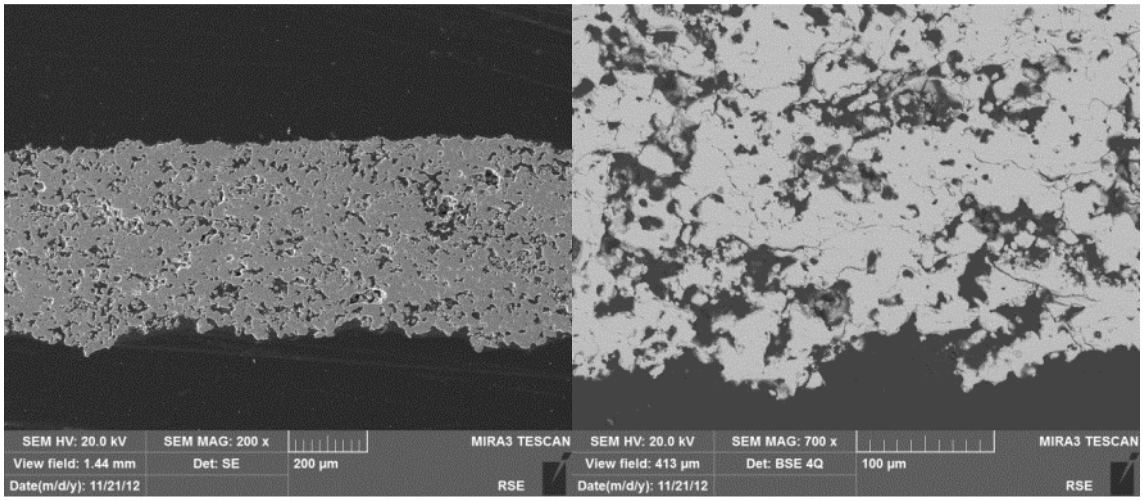

(a) **(b)**

Figure 16. Sample R320-6 (aged @1200°C for 500h) Images at two different magnifications of the section of the TBC.

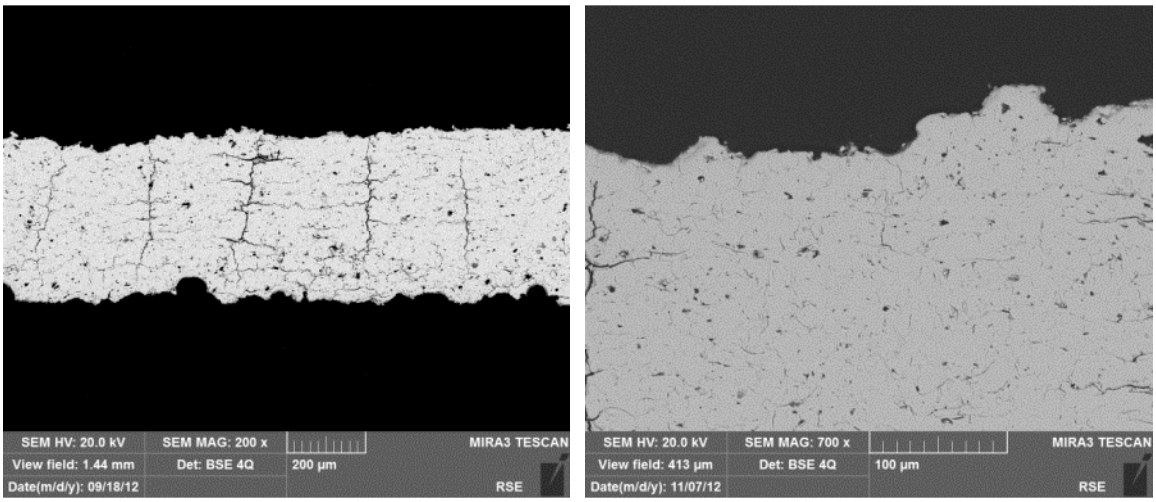

(a) **(b)**

Figure 17. Sample R251-2 (as sprayed) Images at two different magnifications of the section of the TBC. The vertical crack network is clearly visible at lower magnification (crack density 3.5 mm^{-1}).

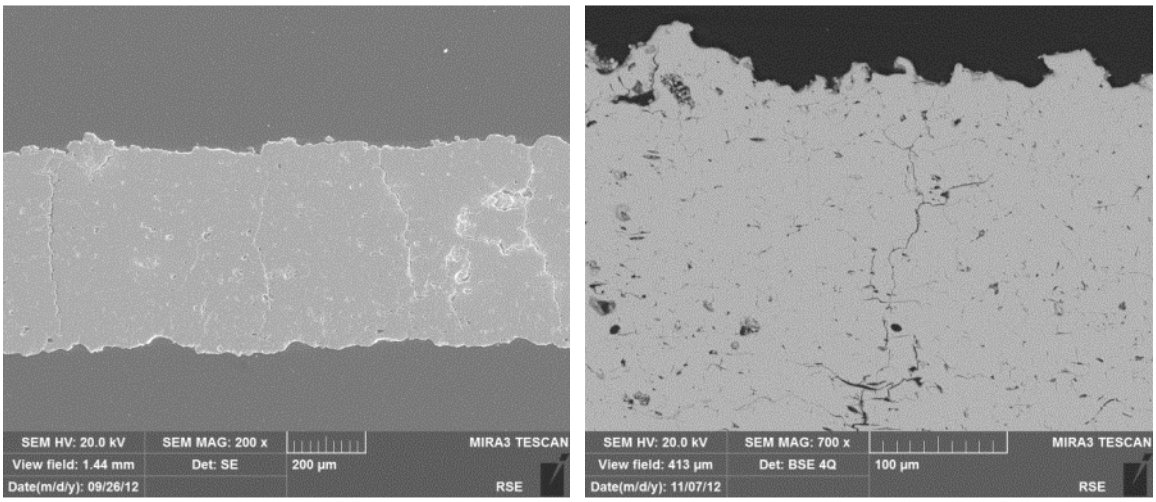

(a) **(b)**

Figure 18. Sample R267-6 (aged @1200°C for 500h) Images at two different magnifications of the section of the TBC. The vertical crack network is clearly visible at lower magnification.

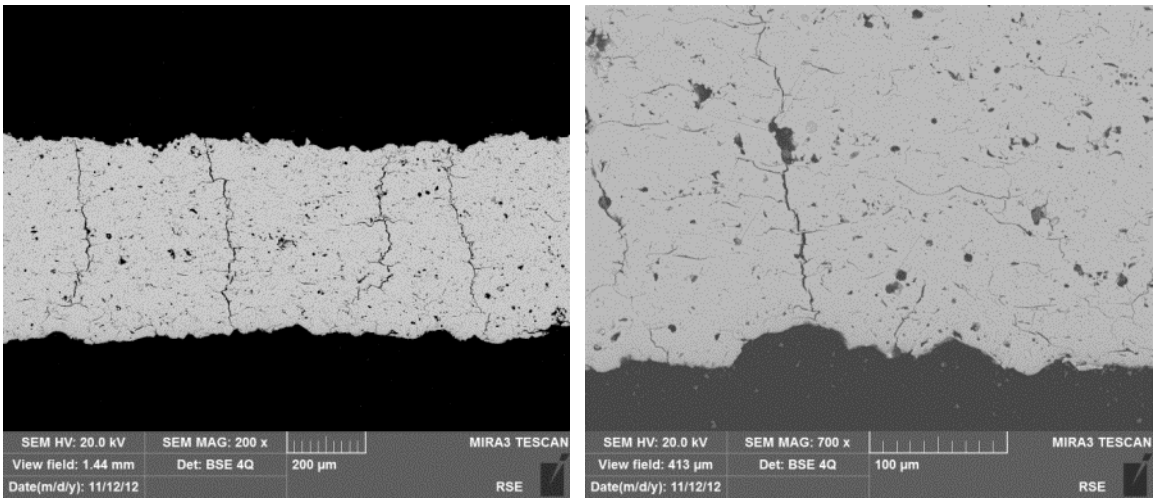

(a) **(b)**

Figure 19. Sample R267-7 (aged @1250°C for 500h) Images at two different magnifications of the section of the TBC. The vertical crack network is clearly visible at lower magnification.

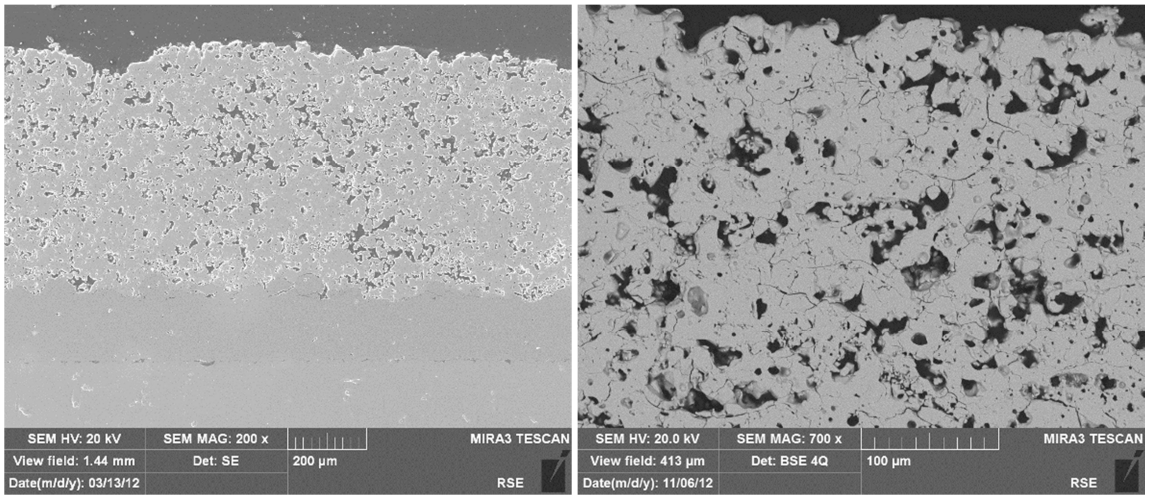

(a) **(b)**

Figure 20. Sample 245-1 (as sprayed). Images at two different magnifications of the section of the TBC.

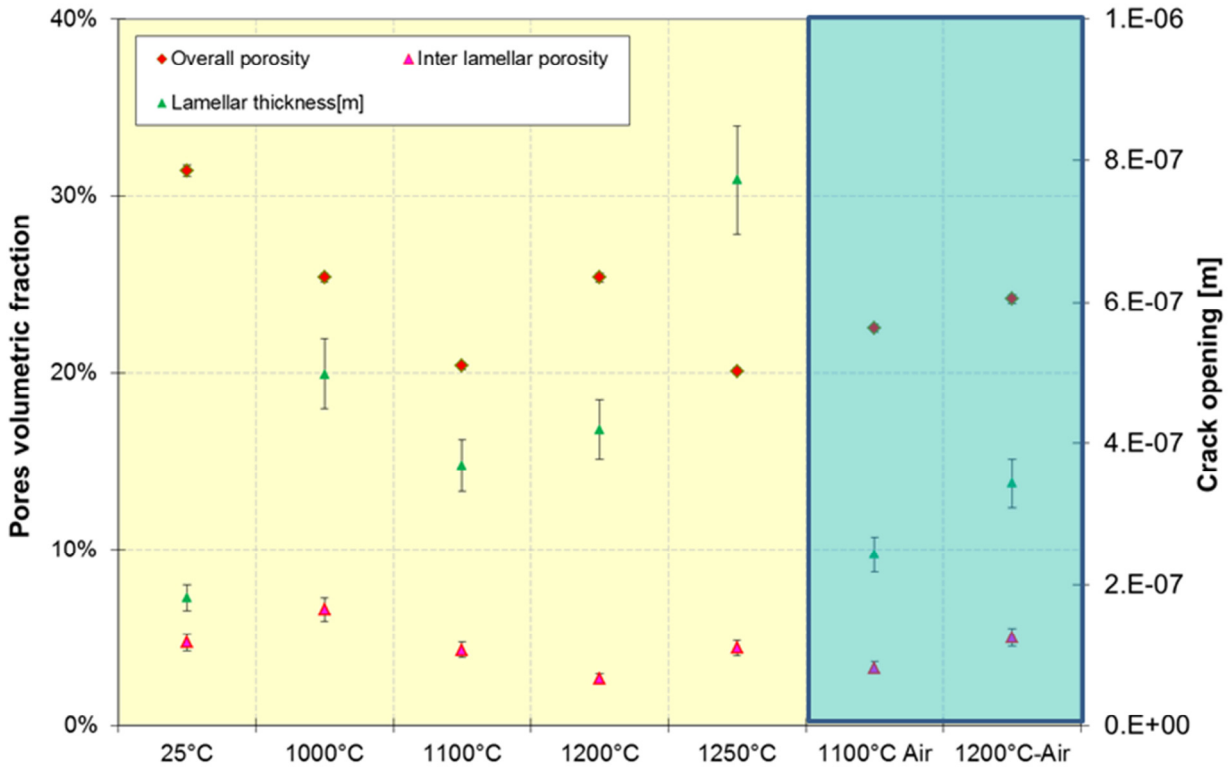

Figure 21. Samples R286, R287 and 320. Overall and inter-lamellar porosity content and thickness as a function of ageing temperature.

Figure 10 - Figure 20 show the microstructure as a function of the aging temperature. In particular, for the standard porous TBC partial sintering is observed as reduction of the overall porosity content (see also Table 4); although a reduction of inter-lamellar pores and intra lamellar cracks can be observed in pictures this is not directly quantifiable by quantitative image analysis as shown in Figure 21 and Table 4.
Comparing the microstructure of as sprayed samples R245 (Figure 20) and R286-1 (Figure 10) a significant difference between the two can be observed in terms of porosity content and morphology (see also Table 4), although they have been deposited using the similar spraying parameters.

Comparing sample aged at the same temperature but in different atmospheres (i.e. air or air+20% H_2O) the differences observed in terms of overall porosity and lamellar pores content result to be within the spreading of the data from sample to sample. This notwithstanding, it could be interesting to observe that the inter lamellar pore thickness (crack opening) as estimated by IR porosimetry (see §5.4 and Annex 1) seems to increase with the ageing temperature as the result of the spheroidization promoted by sintering phenomena. Although the statistics is very limited it seems that sintering rate for samples aged in air is a little bit slower than that for samples aged in air+H_2O.

In the case of dense vertically cracked TBC, owing to the lower porosity content, the sintering phenomena appear less significant (see Table 4 and Figure 17-Figure 19).

5.2.2 Mercury Intrusion Porosimetry (MIP)

MIP facilitates the measurement of a wide range of pore sizes. The results are often expressed in terms of cumulative pore size distribution with pores assumed having cylindrical shape. Real pores are not

cylindrical; they are rather slit-like cracks. But the pressure P required to enter pores, given by the Washburn equation [9]:

$$D = -{}^{4\gamma cos\theta}/_{P} \quad (16)$$

Being D, γ and θ the pore diameter, the surface tension and the wetting angle of Hg, respectively.
Typical information that can be obtained by MIP are specific surface area (SSA) and size distribution. More information on pores evolution can be actually obtained from MIP differential plots which can be derived from the cumulative curves. Often the disappearance of the distribution tail in differential plot indicates complete sintering of small pores, whereas a shift in the distribution maximum provides a measure for pores spheroidizing, i.e. changing in $1/e$ ratio. Area under the curve, as usual, gives the porosity. For the measurements two devices have been used, one for the large pores typically above about 3 µm and one for fine pores below about 3 µm. The used devices are a Pascal 140 and Pascal 440 made by CE instruments (Milan, Italy) operating in a pressure range between 0.008 and 400 MPa corresponding to pore diameters between 3.6 nm and above 100 µm. Measurements have been performed on two as sprayed samples. These give an indication of possible sample to sample variations in pores sizes and specific surface area. Generally, a complexity of TBCs microstructure such as the presence of ink-bottle type pores, non-uniform cross-section of pores, large surface roughness of the samples and associated hysteresis in MIP curves, makes interpretation of MIP data extremely difficult [10 - 12] and the MIP results may contain significant uncertainties.
In general, interpretation of these effects is extremely difficult [13, 14]. General observation for TBCs is that these effects can be suppressed by smoothing of the tail of the MIP differential plots. Ink-bottle can be analysed only approximately [11].
The cumulative plot (see Figure 22) of both standard porous samples show similar overall porosity content. It is worth noting that most of the porosity content (i.e. absolute value higher than 20%) is related to coarse pores wider than 1 µm radius. Fine (0.1µm<r<1µm) and very fine (0.1>r) pores are responsible for 5.7% and 1 – 2.4% of porosity, respectively.
The significant difference of very fine porosity content of the two samples can be perhaps ascribed to the presence of some bottle necks generating artefacts (i.e. a wide pore connected to the others through a fine neck).
The smoothed differential plot (see Figure 23) clearly shows that the two samples are more or less similar (same peak position corresponding to pore radius of about 2.75 µm) apart a very fine pore contribution previously discussed (see the very narrow peak on the left side of the figure).
These results are in good agreement with those obtained by quantitative IA, in fact since most of the coarse porosity in MIP plots can be considered globular, as also confirmed by the microscopy images, values for coarse (MIP) and globular (IA) pores differ within the experimental uncertainty related to each experimental technique. Of course overall porosity values obtained by MIP and IA can also differ owing to the presence of some pores closed to mercury intrusion that can observed by IA.
As concern the specific surface area (SSA) the significant difference between the two samples (see Figure 24) is clearly related to the contribution of very fine porosity for sample R286-1. Since it is not clear whether this contribution is real or an artefact a more reliable estimation of SSA for this sample would exclude the contribution of very fine porosity (Log(r)<-2.15) that results close to four times that of the other pores. By this way SSA ranges from $1 \cdot 10^6 m^2/m^3$ (R286-1) to $1.64 \cdot 10^6 m^2/m^3$ (R286-1bis)

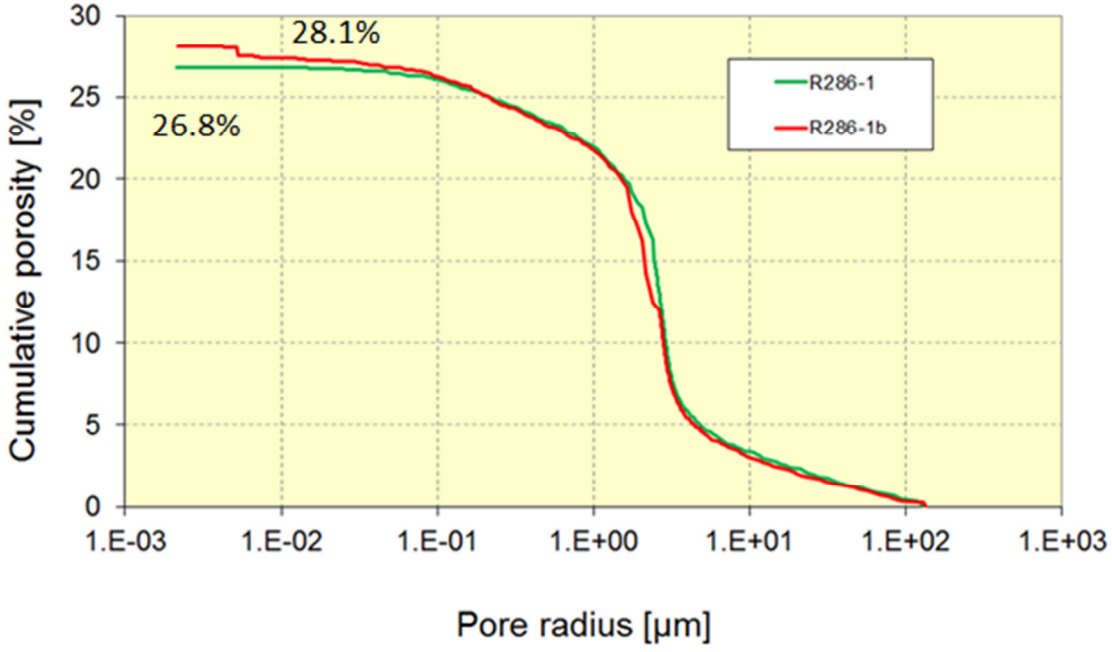

Figure 22. Cumulative MIP plots vs. pore radius for the two as sprayed standard porous TBC samples. More than 20% of porosity seems to be made of coarse pores bigger than 1 µm.

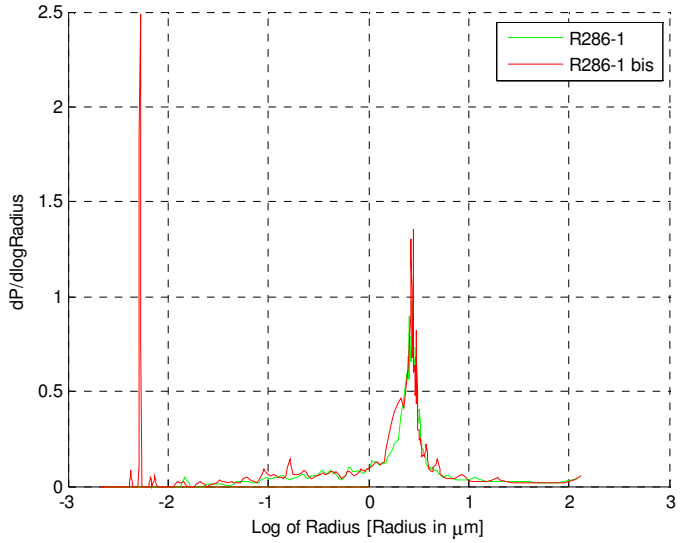

Figure 23. Samples R286-1 and R286-1bis. MIP differential plot.

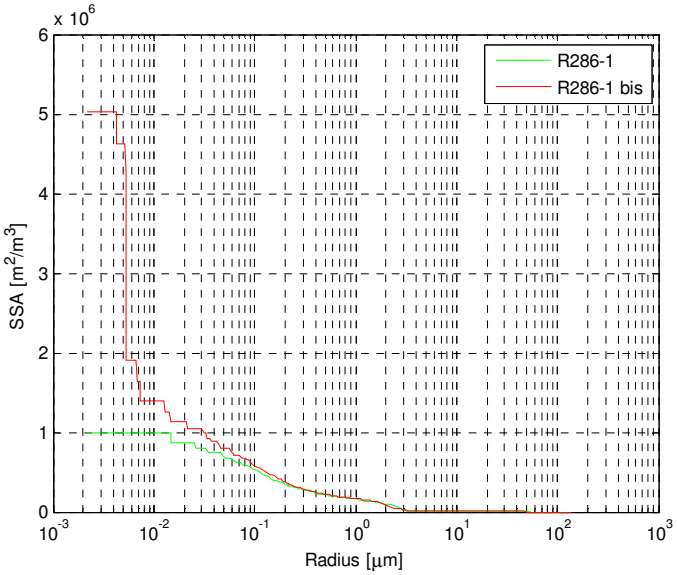

Figure 24 Samples R286-1 and R286-1bis. Specific surface area plot.

5.3 Thermal diffusivity measurement

In the following the results of all the thermal diffusivity measurements performed at RT and at high temperatures are reported.
Results of thermal diffusivity measurements carried out using different gases (He, Ar and N_2) at different pressures (0.25 bar, 0.5 bar, 0.75 bar and 0.9 bar) and high vacuum (<$1 \cdot 10^{-8}$ bar) are reported in a dedicated section as these data were used to characterise inter-lamellar pores according to a technique (IR porosimetry) shortly described in Annex 1.

5.3.1 Thermal diffusivity at RT in air and in vacuum

In this section are reported only data referring to measurements carried out at RT in air and in vacuum for comparison purposes with data obtained in WP2.3 section as well as with literature.
Data obtained at RT can furnish several useful information on the TBC. First of all, the thermal diffusivity of as sprayed coatings gives an idea of what type of TBC is measured. Depending on their microstructure, for standard porous and vertically cracked TBC, typical values for RT thermal diffusivity measured in air are 3 – 4.5 10^{-7} m^2/s and 4.5 – 6 10^{-7} m^2/s, respectively [8, 18, 19].
In this specific case, in agreement with the literature, as summarised by Table 5, standard porous and vertically cracked TBC show average values of $3.86 \cdot 10^{-7}$ m^2/s and $4.82 \cdot 10^{-7}$ m^2/s, respectively.
Another parameter that can be obtained is the ratio between thermal diffusivity measured in vacuum and in air. In fact depending on the microstructure, this ratio can change even significantly. The asymptotic value for this ratio is 1. The pores that mainly contribute to this ratio are of course the open pores (those that are affected by having a different medium inside: air or vacuum). Among all the open pores, inter-lamellar pores laying in planes parallel to the TBC surface are those that mainly affect the through the thickness thermal diffusivity[2]. In particular, owing to the Knudsen effect (see Annex 1 for details) those that are more sensitive to the gas inside are the thicker. In fact, as shown in Figure 25, for cracks thicknesses thicker than 2-3 µm the drop of the thermal conductivity is limited. On the other hand, for very thin cracks (<0.05 µm) the thermal conductivity of the gas inside the pore is very low even when filled with gas.
Thus an increase of the ratio $\alpha_{vacuum}/\alpha_{air}$could means that there is:

- an increase of closed pores;
- an increase of very thin pores;
- a reduction of horizontal inter-lamellar pores.
- a spheroidization of pores.

High temperature exposure usually promotes the spheroidization of pores and the partial or complete sintering of the finest fraction of inter- and intra- lamellar pores. On the contrary, it is unusual to observe an increase of very fine pores and cracks especially for free standing coatings. Obviously, partial sintering could also close some path towards pores increasing the volumetric fraction of closed pores.
Thus an increase of the ratio can be mainly ascribed to reduction/spheroidization of inter-lamellar pores and perhaps an increase of the close pore fraction. For estimating the presence of closed pores the overall porosity estimated by IA should be compared to the MIP results.
Very often, data available in the literature refer to different ageing times and temperatures. For comparison purposes it is useful to introduce the Larson Miller parameter (LMP) merging together time *t* and temperature *T*::

$$\mathrm{LMP} = T(K) \cdot \left(\ln(t(h)+1) + 20\right) \tag{17}$$

already successfully used for several decades in describing the evolution of mechanical properties of metals as a function of time and temperature of ageing.

[2] For an example of the effects of spherical pores the ratio for a TBC having 25% spherical porosity with 3 µm diameter is 0.99. On the contrary 10% of lamellar pores with 1 micron thickness and 1/40 aspect ratio is 0.31.

Figure 26 shows the $\alpha_{vacuum}/\alpha_{air}$ as a function of LMP. For comparison purposes in the same figure are reported also literature data [8, 20]. The main difference between the data of the present work and literature is that the latter refer to porous TBC aged for different times at the same temperature (1250°C) while the former refer to different ageing temperatures (1000 – 1250°C) for the same time (500 hours).
This could be a possible explanation for the difference in the slope shown by R287 samples and literature. In fact, although LMP could help to compare results coming from tests performed in different conditions, the sintering phenomena are not affected by time and temperature exactly as supposed considering LMP. This means the shorter ageing times at higher temperatures can promote a more significant spheroidization/sintering of pores compared to that resulting from a longer time but a lower temperature.
The values of the ratio $\alpha_{vacuum}/\alpha_{air}$ for dense vertically cracked samples (R267) result always higher than the corresponding one for standard porous (R287& R320), as reasonable because of the lower inter-lamellar porosity content.

Table 5 RT thermal diffusivity measurements in air and vacuum

Sample code	TBC type	Aging T [°C]	Aging Env.	RT thermal diffusivity vacuum[3] [m²/s]	RT thermal diffusivity air [m²/s]	Ratio Vacuum/ air	Expected thermal diffusivity increase	Measured Thermal diffusivity increase
R286-1	SP/F	As sprayed	n.a	2.67±0.02E-7	3.65±0.03E-7	0.75	n.a	n.a
R286-5	SP/F	As sprayed	n.a	3.01±0.02E-7	4.01±0.03E-7	0.73	n.a	n.a
R287-1	SP/F	1000	Air+20 % H2O	2.99±0.02E-7	4.14±0.02E-07	0.72	1.42	1.07
R287-5	SP/F	1100	Air+20 % H2O	3.46±0.03E-7	4.35±0.03E-07	0.79	1.63	1.15
R287-9	SP/F	1200	Air+20 % H2O	4.86±0.03E-7	5.77±0.05E-07	0.84	1.83	1.51
R287-10	SP/F	1250	Air+20 % H2O	4.82±0.03E-7	5.31±0.05E-07	0.91	1.93	1.38
R251-2	VC/F	As sprayed	Air+20 % H2O	3.95±0.03E-7	4.82±0.05E-7	0.82	n.a	n.a
R267-6	VC/F	1200	Air+20 % H2O	7.0±0.2E-7	7.6±0.3E-7	0.92	1.66	1.58
R267-7	VC/F	1250	Air+20 % H2O	6.57±0.08E-7	6.89±0.08E-7	0.95	1.75	1.44
R320-1	SP/F	1100	Air	3.14±0.03E-07	4.18±0.04E-7	0.75	1.63	1.09
R320-6	SP/F	1200	Air	3.92±0.03E-07	4.76±0.05E-7	0.82	1.83	1.24
R245-1	SP	As sprayed	Air	n.a		n.a		

The ratio *r*, the thermal diffusivity after ageing normalised in respect to the as sprayed value, is another possible parameter for studying the sintering of TBC. In this case independently from the environment inside the pores the value of this ratio is expected to monotonically (but not linearly) increase as a function of time and/or temperature owing to sintering phenomena occurring at high temperatures. Obviously the higher the non-globular fine pores content in the TBC, the higher the increase of thermal diffusivity for a certain ageing time and temperature. Also in this case, LMP is a good way for comparing data referring to different experimental situations. In Table 5 and in Figure 27 is reported the

[3] The experimental uncertainty is that obtained performing five consecutive measurements, usually the reproducibility of thermal diffusivity by laser flash and thermographic techniques in of the order of ±5%.

ratio *r* as a function of LMP for samples sets R287, R320, R267 and R245, R269 and R270 cyclic aged at 1080°C in the frame of the WP2.3. For comparison purposes literature data have been also included in the figure.

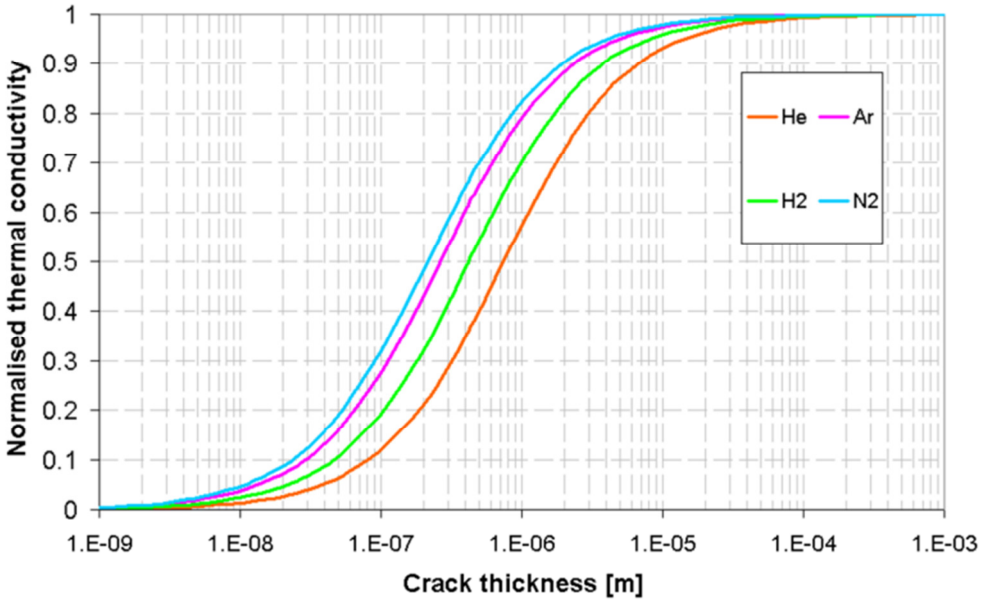

Figure 25. Normalised thermal conductivity of four different gases when inside a two parallel planes separated by a certain thickness (crack thickness).

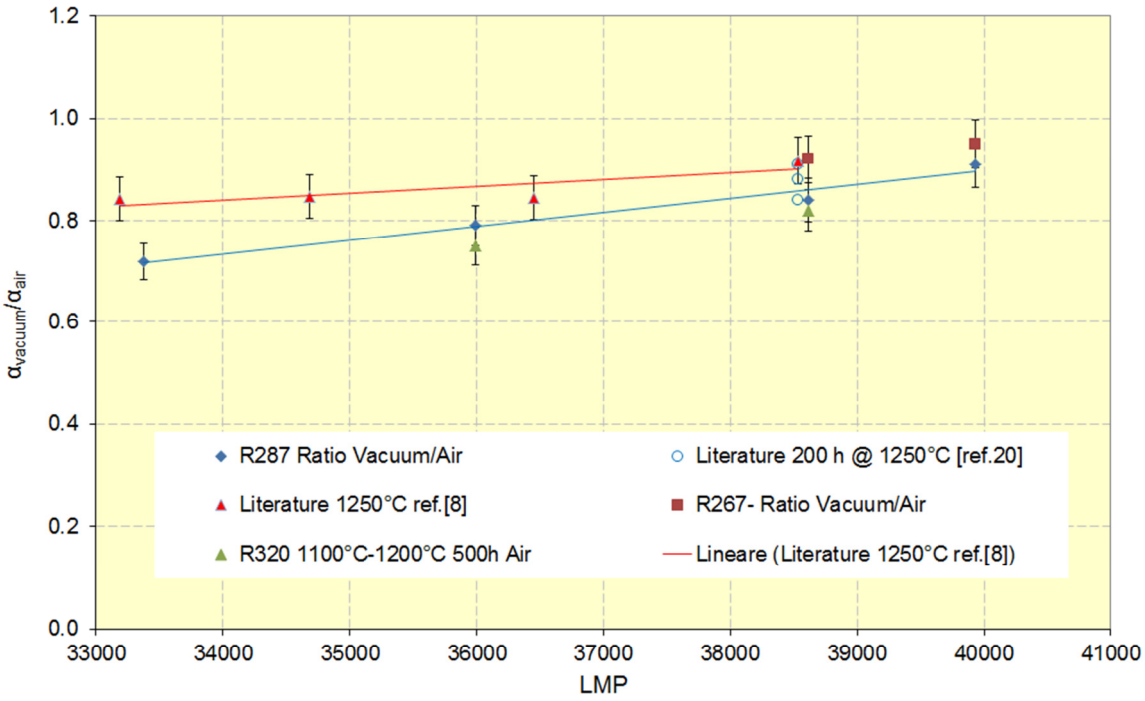

Figure 26. Ratio $\alpha_{vacuum}/\alpha_{air}$ as a function of the LMP for the two sets of TBC samples (R287-R320 and 267). A comparison with literature data is also reported.

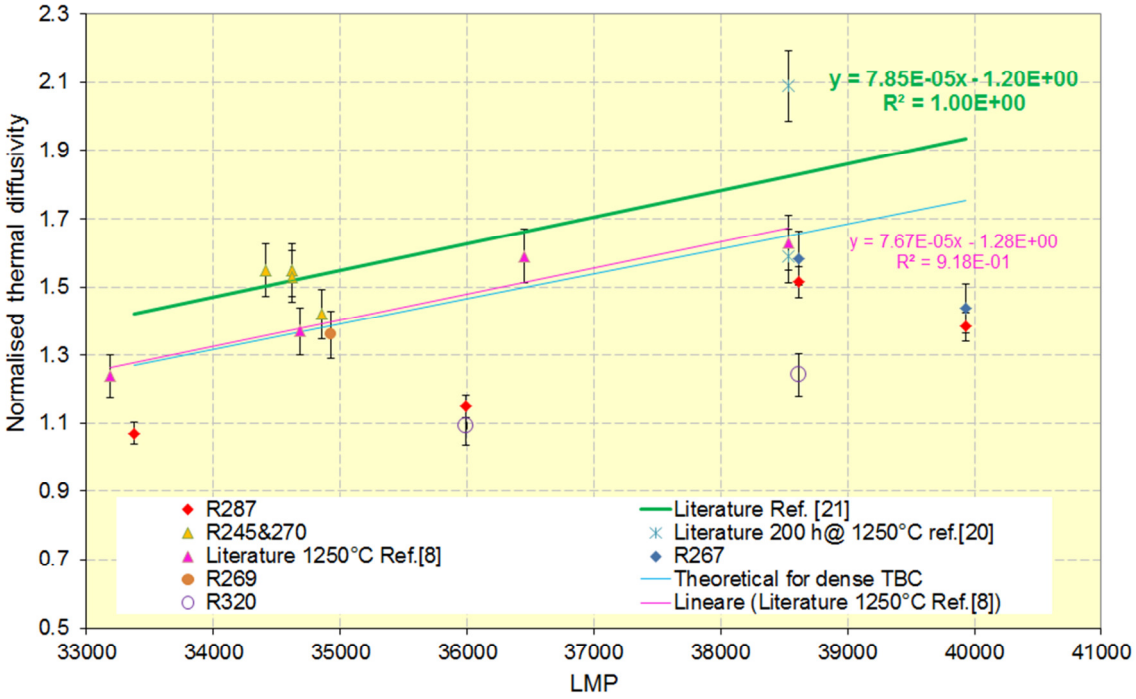

Figure 27. Normalised thermal diffusivity as a function of LMP.

Looking to the experimental results there are the following points to highlight:

- Porous samples (R287&R320) seem to sinter less compared to literature values (green and magenta lines) and sets R245&270;
- Samples R320 aged in air seems to sinter within the typical scatter of data as those aged in air+steam (R287);
- Dense vertically cracked samples (R267) sinter slightly more than porous samples (R287);
- Both porous (R287) and dense vertically cracked (R267) samples aged at 1250°C show a lower normalised thermal diffusivity value compared to that at 1200°C.

For the latter point, a possible explanation for the results should be related to effects non related to sintering but probably to unbalanced phase transformations or chemical reactions (for example with H_2 if steam dissolution occurs). In fact both porous and dense TBC at 1250°C show a decrease of thermal diffusivity compared to the value at 1200°C but the sintering ratio is linearly increasing even at 1250°C, as shown in Figure 26.
The lower sintering rate of R287 TBCs (compared to literature and other TBC sets, apart from R320) could be caused by its very porous microstructure made mainly of globular voids that differs from that of TBC sets R270 and R245.
As concerns phase transformation, it is well known that during operation some phase transformation of YPSZ occurs but this is usually considered neutral from the thermal diffusivity point of view. In fact, high temperature exposure promotes the transformation of tetragonal metastable *t'* YPSZ in low content Yttria stabilised tetragonal *t*-Zirconia plus high content tetragonal phase *t1'* and cubic *c* fully stabilised zirconia. Longer times and/or higher temperatures promote the formation of monoclinic zirconia as well, as reported in the literature and shown in Figure 28. Comparing the average values for the thermal conductivity of single crystal YPSZ phases and considering the relative weights of cubic *c* and tetragonal phases along the ageing, the resulting thermal conductivity of the mixture of different phases in aged YPSZ appears only slightly affected by these phase transformations. To quantify the effect of ageing on the thermal conductivity of bulk YPSZ considering LMP is a reasonably good parameter for comparing results of ageing performed at different temperatures for different times, we considered the phase composition reported in the literature [28] for LMP values as close as possible to the value

corresponding to 500 hours at 1250°C. Table 7 reports the thermal conductivity as estimated by this approach. The first column report the data available in the literature as well as the time needed to have exactly the same LMP as 1250°C for 500h.

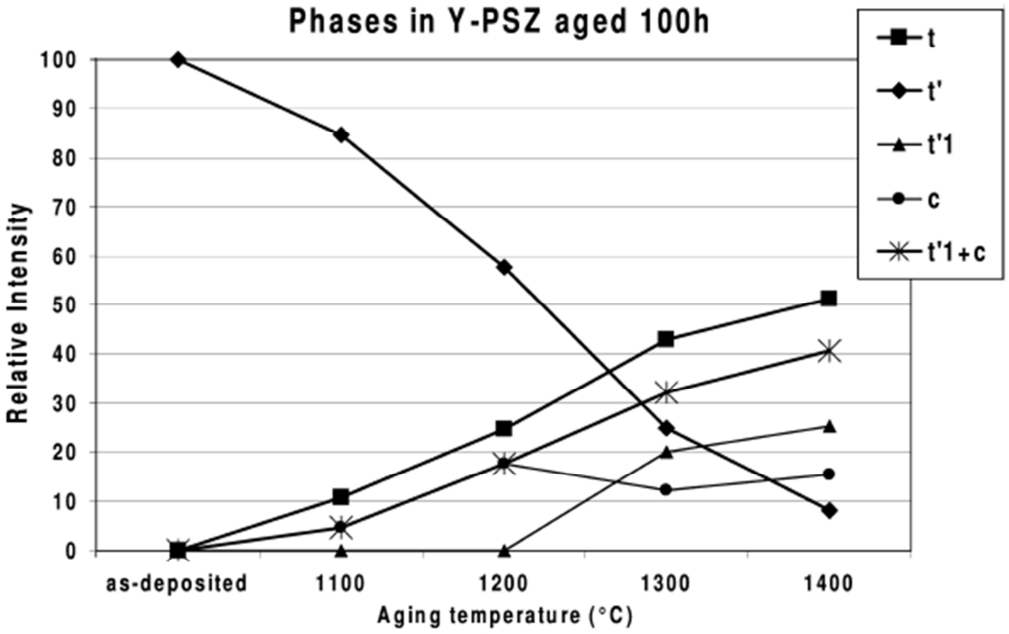

Figure 28. Relative intensities of the different phases in YPSZ as a function of the ageing temperature (the time is fixed equal to 100 hours) as measured by X ray diffraction [23].

Table 6 Thermal conductivity values for the different phases of single crystal YPSZ

Thermal conductivity [W/mK]	t'	t	t'1	c
Youngblood et al. [22]	2.5	2.8	2.3	2
Schlichting et al. [27]		3	1.8	
Azzopardi et al.[23]	2.6			1.8
Mevrel et al. [25]				
Bisson et al. [24]	2.9			2.1
Miller at al. NASA policrystal [26]	2.5			
Mean values	**2.63**	**2.90**	**2.05**	**1.97**

Table 7 Two examples of the estimation of thermal conductivity of YPSZ as a function of ageing time and temperatures.

Ageing time and temperature	*t'*	*t*	*c*	Estimated thermal conductivity of the mixture [W/mK]
1000 h 1200°C (correct time 1217h)	27.1%	49.2%	23.7%	2.61
100 h 1300°C (correct time 217 h)	28.3%	49.6%	22.1%	2.62

5.3.2 Thermal diffusivity measurement as a function of the temperature

Figure 29 and Figure 30 show the experimental thermal diffusivity measured vs. the temperature for the two state of the art TBCs considered in the frame of this project.

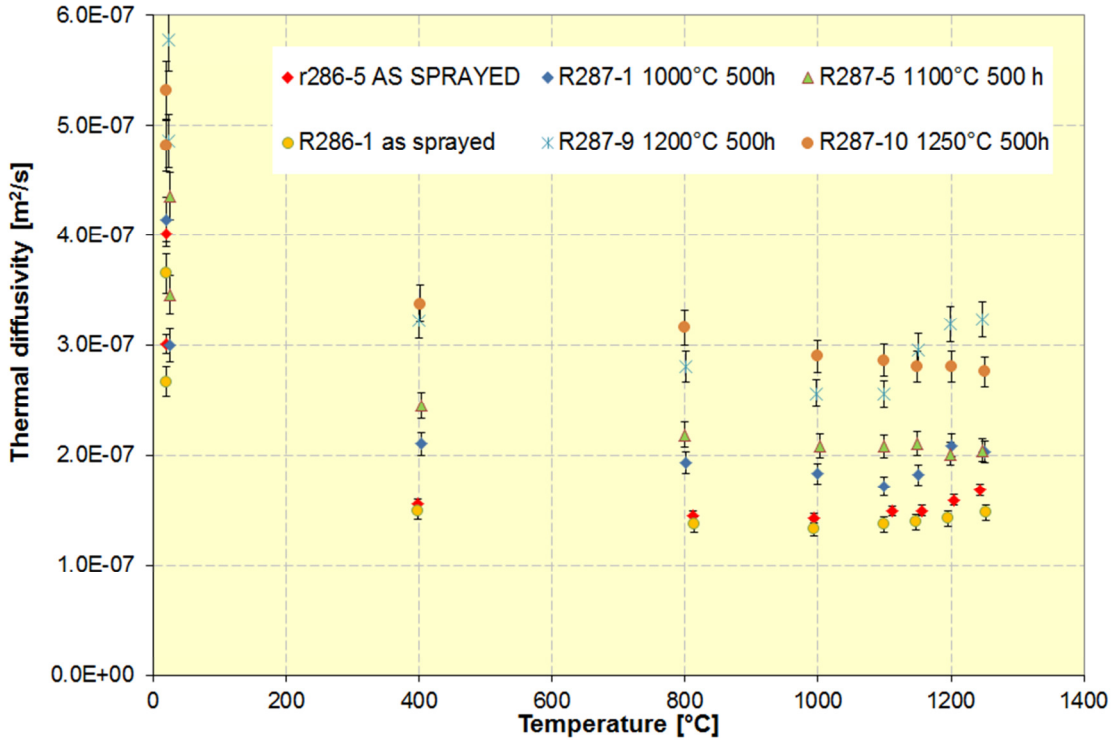

Figure 29. Samples R287. Thermal diffusivity as a function of the temperature.

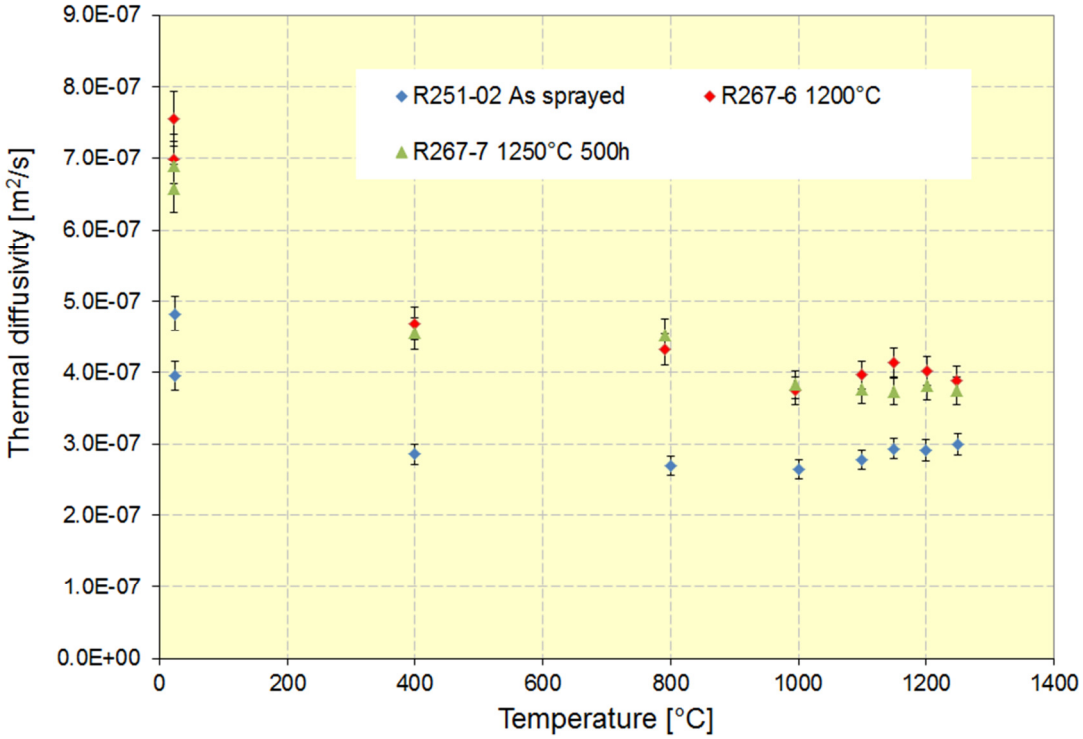

Figure 30. Samples R251&267. Thermal diffusivity as a function of the temperature.

It is worth noting that for both standard porous and dense vertically cracked samples the thermal diffusivity shows the typical trend as a function of temperature. In particular, after an initial decrease vs. temperature typical for materials (such as YPSZ) where phonons are the responsible for the heat transfer, an increase can be observed from about 1000°C, owing to the through-the-thickness radiative contribution to the heat transfer that takes place and start to be relevant. In fact, YPSZ is translucent to visible and near infrared radiation[4]. Only for very few samples this trend is not pronounced.
As expected due to sintering phenomena taking place at high temperature thermal diffusivity values increase as a function at the ageing temperature. As also previously highlighted, this is always true but not for the samples aged at the highest temperature (i.e. 1250°C). In fact, in both figures thermal diffusivity values are lower or at least comparable to those of samples aged at 1200°C.

5.4 Microstructural evolution as detected by IR porosimetry

As explained in details within Annex 1, by measuring thermal diffusivity of TBC having gases with different thermal and fluid-dynamical properties at different pressure could be a way to obtain some effective averaged microstructural parameters of inter-lamellar pores because they are the pores that most significantly affect the through-the-thickness thermal diffusivity. The two parameters that have been decided to extract by inverting the experimental thermal diffusivity data are the inter-lamellar pore thickness l and the aspect ratio a/c. Coupling these data with porosity data furnished by image analysis, it is possible to estimate also the specific surface area of the porous TBC.
The outcomes of this study are summarised in Figure 21 and Figure 31.
Although some fluctuations from sample to sample inter-lamellar aspect ratio and thickness show an increase as a function of ageing temperature as expected owing to spheroidization promoted by sintering.
As a results of the increase of both these two parameters, the estimated specific surface area (SSA) significantly decreases with the ageing temperature. It is also worth noting that the estimated value for

[4] The wavelength corresponding to the peak of the black body radiation curve at 1000°C is about 2.2 µm.

the as sprayed sample is in good agreement with the value measured by MIP. Furthermore, the two samples aged in air show a smaller SSA decrease and aspect ratio *a/c* increase.

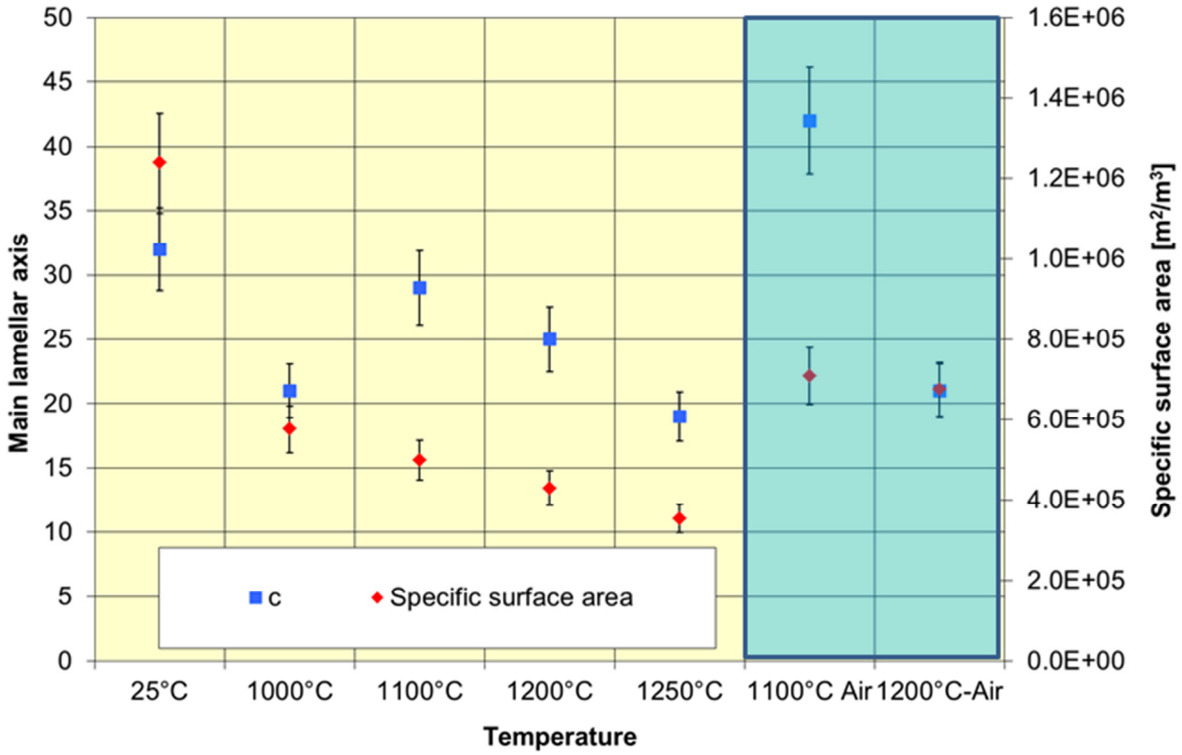

Figure 31. The reciprocal of the aspect ratio a/c (i.e. the main lamellar axis) and the specific surface area as estimated by IR porosimetry.

5.5 Specific heat measurements

On an as sprayed TBC (samples R286-1b) the specific heat was measured setting two different heating rates (4K/min and 10K/min) to assess the independence of specific heat from the heating ramp value. Figure 32 shows that as expected no significant differences can be observed between the two experimental curves. A satisfactory agreement between experimental and literature curves for the sapphire reference and YPSZ sample is observed.

Specific heat measurement have been performed also on samples aged in air+H_2O, as shown in Figure 33. The specific heat data of aged samples seem to be slightly lower than those reported in the literature, but in any case within the typical experimental uncertainty for specific heat measurements. it is worth noting that specific heat is not expected to change significantly as a function of the stabiliser (Y_2O_3) and thus of the crystalline phase [23].

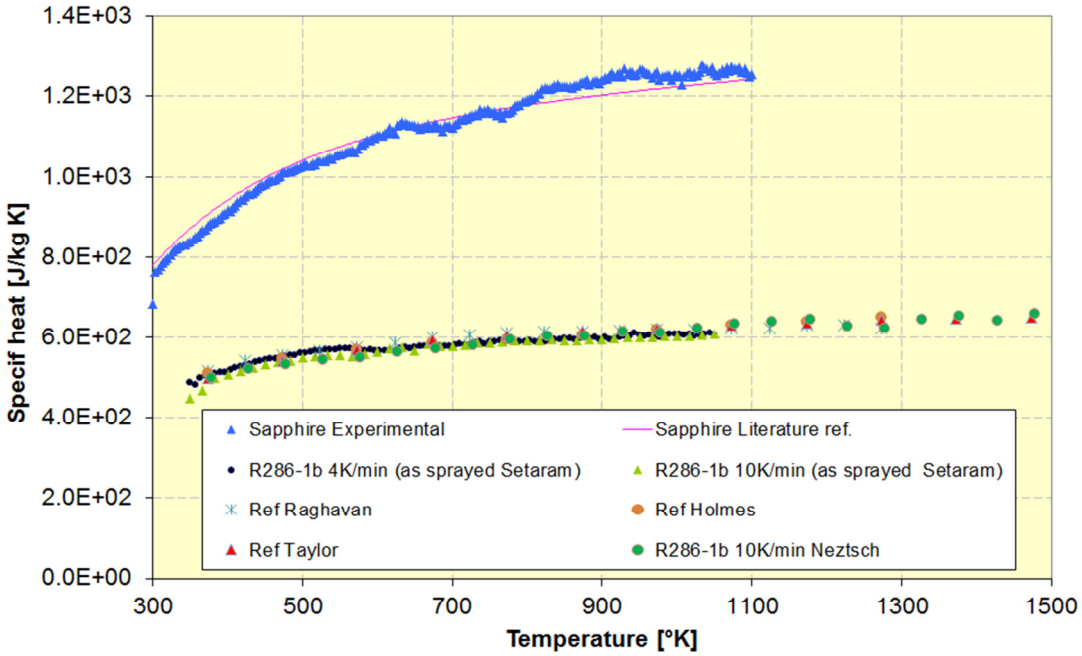

Figure 32. Sample R286-1b. Specific heat curves as a function of temperature for two different heating rates. For comparison purposes the literature and the experimental curves for the sapphire used as reference sample and YPSZ are reported as well.

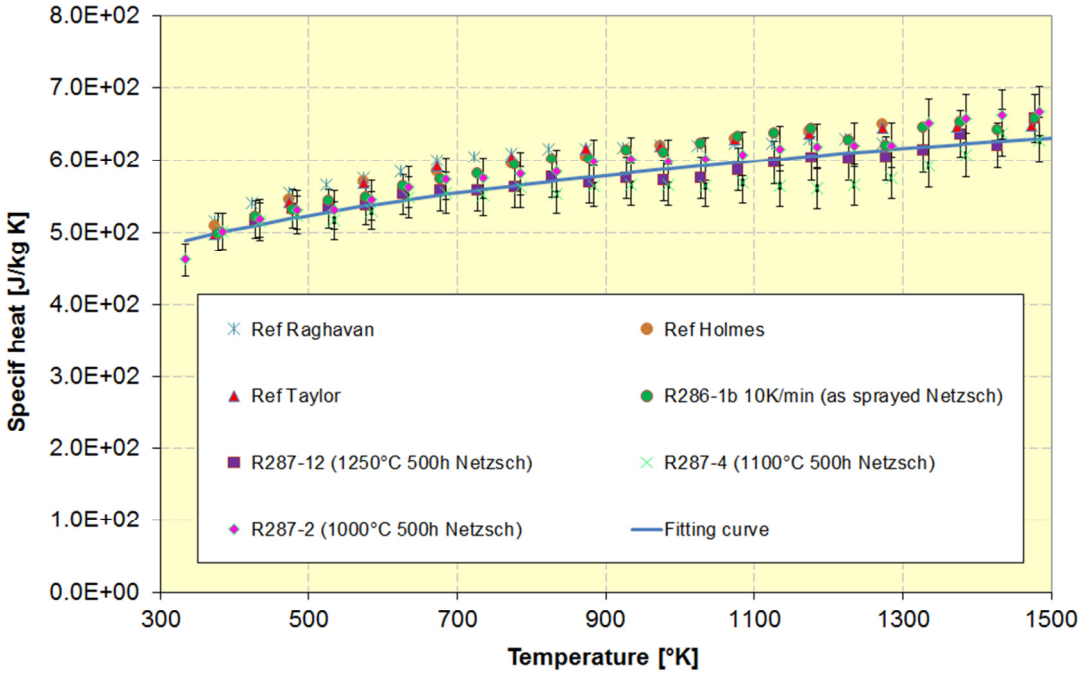

Figure 33. Aged samples. Specific heat as a function of temperature. For comparison purposes YPSZ literature curves are reported.

5.6 Thermal conductivity estimation

Thermal conductivity k has been estimated taking into account that:

$$k = \alpha \cdot \rho \cdot C_p \tag{18}$$

Density has been estimated from the porosity value f measured by image analysis as:

$$\rho = \rho_{bulk}(1 - f) \tag{19}$$

assuming a bulk density ρ_{bulk} of 6050 kg/m^3. When density at high temperature has to be considered, according to literature a thermal expansion coefficient equal to $1 \cdot 10^{-5}/C°$ has been assumed.
For each temperature the specific heat C_p has been estimated by using the curve fitting the experimental data shown in Figure 33.
Figure 34and Figure 35 report the thermal conductivity values as a function of temperature, as measured in vacuum. The uncertainty has been obtained by propagating the experimental uncertainty of each parameter in eq.(18) and eq.(19).

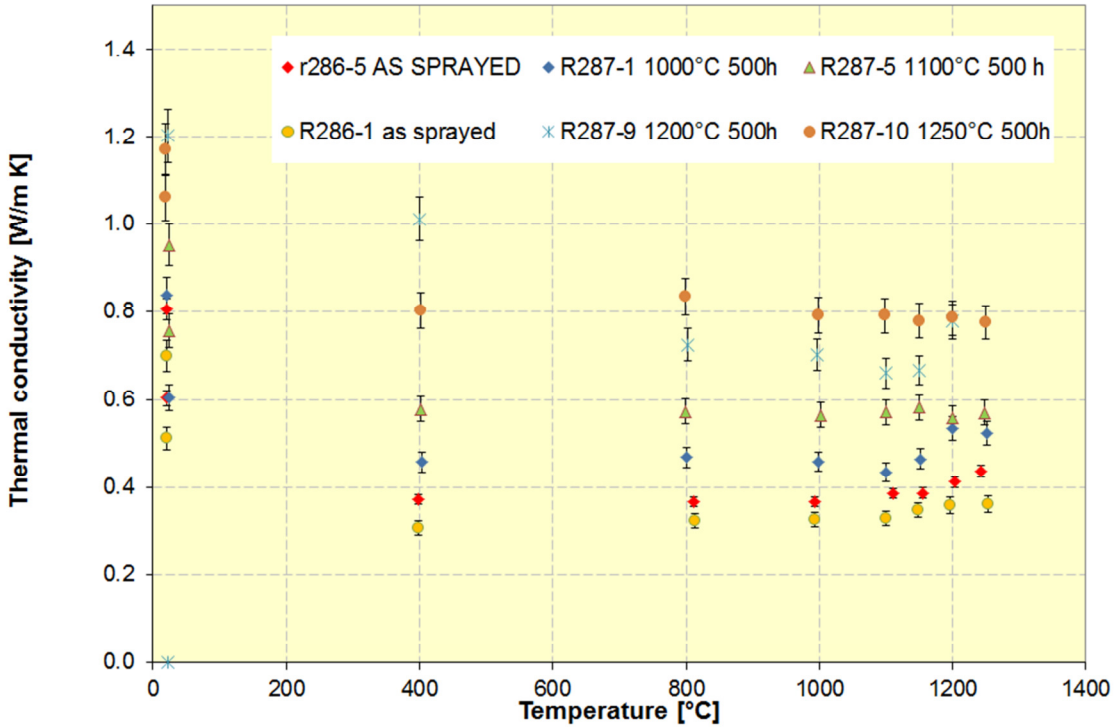

Figure 34. Samples R287. Thermal conductivity as a function of the temperature.

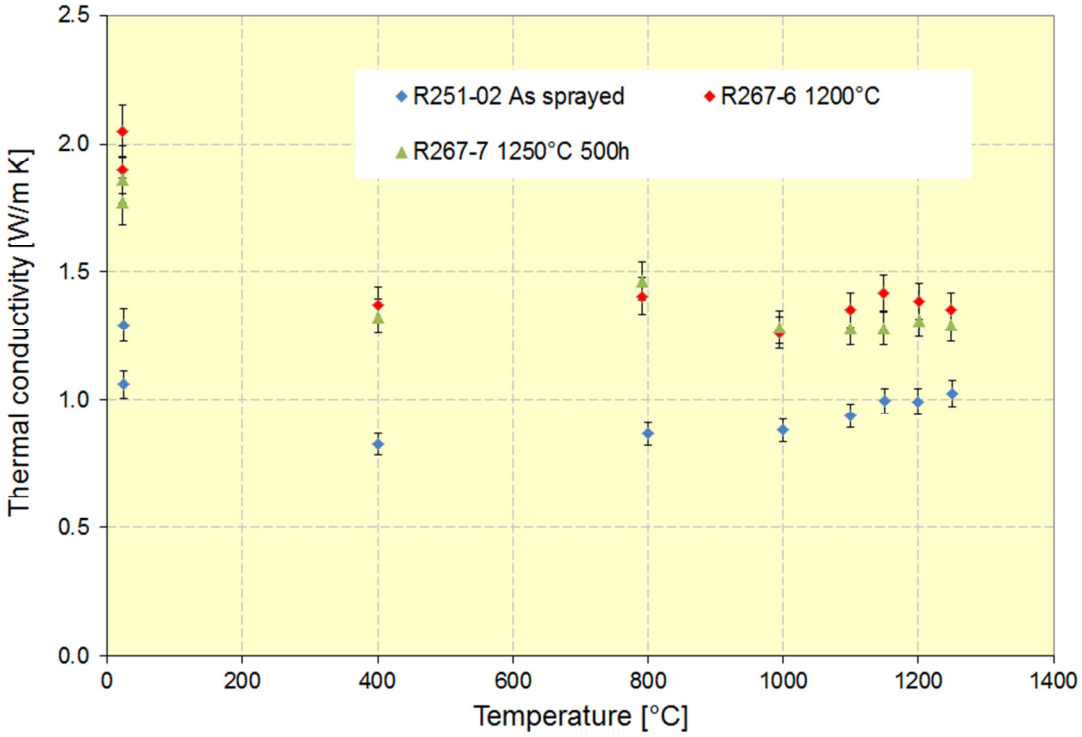

Figure 35. Samples R251&267. Thermal conductivity as a function of the temperature.

6 CONCLUSIVE REMARKS

The main outcomes of this activity are:

- The porous TBC samples supplied for the thermo-physical characterisation exhibit a very porous microstructure (30%), constituted mainly by wide globular pores, compared to those of the other porous TBC (20%) supplied for other purposes in the frame of the project.
- Thermal diffusivity and conductivity of both porous and dense vertically cracked TBC resulted within typical ranges reported in the literature, although a smaller sintering rate, probably caused by the globular geometry of most of the pores, is observed.
- Typical trend of thermal diffusivity/(conductivity) as a function of temperature has been observed for the tested samples.
- Thermal diffusivity of samples aged at 1250°C resulted slightly smaller than those of samples aged at 1200°C. Possible explanations for this occurrence are:
    - The two samples aged at 1250°C had as sprayed thermal diffusivity values lower than those measured on as sprayed samples (in particular, for the porous TBC an as sprayed value equal to $3.05 \cdot 10^{-7}$ m^2/s, which is within the typical range variability, has to be supposed)
    - At 1250°C some interactions between the ageing environment and the TBC took place. This point will be clarified in the frame of the activities which will carried out within WP2.4.
- The specific heat data are in good agreement (within the experimental uncertainty) with values reported in the literature and no effects of both ageing temperature and environment have been observed.

7 REFERENCES

1. W.P. Parker, R.J. Jenkins, C. P. Butter G. L. Gutter and G.L. Abbott, *J. Appl. Phys*., 32, pp.1679, (1961).
2. ASTM Standard E1461.
3. R.E. Taylor, K.D. Maglic, *Compendium of Thermophysical Property Measurement Methods* Vol: 1: Survey of Measurement Techniques, Eds. K.D. Maglic et Al. Plenum Press New York 1984.
4. R.E. Taylor, K.D. Maglic, *Compendium of Thermophysical Property Measurement Methods* Vol: 2: recommended Measurement Techniques and Practices, Eds. K.D. Maglic et Al. Plenum Press New York 1992.
5. I. Philippi, J.C. Batsale, D. Maillet and A. Degiovanni. Measurement of thermal diffusivities through processing of infrared images. Rev. Sci. Instrum. 66 (1), January 1995.
6. D. Maillet, S. André, J.C. Batsale, A. Degiovanni, C. Moyne. *Thermal Quadrupoles*. Wiley & sons, 2000.
7. H. Stehfest, Numerical invertion of Laplace transforms, Communications of the ACM, Vol. 13 (1) January 1970.
8. Cernuschi F., Bison P.G., Martinetti S., Scardi P., Acta Mater 2008; 56: 4477 –88
9. Washburn E. W., Proc. Natl. Acad. Sci. USA., 1921; 7: 115-6.
10. Siebert B., Funke C., Vassen R., Stoever D., J. Mater Processing Technology, 1999; 92 – 93; 217-23.
11. Paul S., Pore Architecture in Ceramic Thermal Barrier Coatings, PhD thesis, University of Cambridge, Department of Materials Science, 2007.
12. Paul S., Cipitria A., Golosnoy I.O., Xie L., Dorfman M.R., and Clyne T.W., J. Therm. Spray Technol. 2007; 16:798-803.
13. Makri P. K., Stefanopoulos K. L., Mitropoulos A. C., Kanellopoulos N. K., and Treimer W., Physica B, 2000; 276: 479-80.
14. Ilavsky J., Berndt C. C., and Karthikeyan J, J. Mater. Sci., 1997; 32 (15): 3925-32.
15. S. Raghavan, H. Wang, W.D. Porter, R.B. Dinwiddie, and M.J. Mayo, Acta Mater. 49 (2001) 169179
16. Holmes, R. R. and McKechnie, T. N. In NASA Marshall Space Flight Center Advanced Earth-To-Orbit Propulsion Technology vol 1, eds. Richmond, R.J., Wu, S.T., 1988, pp. 692–702.
17. Taylor, R. E., Wang, X. and Xu, X., Surf. Coat. Technol., 120- 121, 1999, 89–95.
18. D. Schwingel, R. Taylor, T. Haubold, J. Wigren, C. Gualco, Surf. Coat. Technol. 108 – 109 (1998), 99 – 106.
19. P. Bison, F. Cernuschi, S. Capelli, Surf. Coat. Technol. 205, 2011, 3128-3133.
20. F. Cernuschi, I.O. Golosnoy, P. Bison, A. Moscatelli, R. Vassen, H.-P. Bossmann, S. Capelli, Acta Mater., 61, 1, 2013, 248–262.

21. F. Cernuschi, S. Capelli, P. Bison, S. Marinetti, L. Lorenzoni, E. Campagnoli and C. Giolli, Acta Materialia 59 (2011) 6351–6361.

22. Youngblood G.E., Rice R.W., Ingel R.P., J. Am. Ceram. Soc. 1988; 71(4): 255- 60

23. Azzopardi A., Mevrel R., Saint-Ramond B., Olson E., Stiller K., Surf. Coat Technol. 2004; 177 – 178; 131-9.

24. J-F Bisson, D. Fournier, M. Poulain, O. Lavigne, R. Mévrel, J. Am. Ceram. Soc. 83 [8] 1993 – 98 (2000)

25. R. Mévrel, et Al. J. Eur. Ceram. Soc. 24, (2004)

26. R. Miller, S. Zhu, NASA TM 2000-210238

27. K.W. Schlichting, N.P. Padture, E.H. Jordan, M. Gell, Materials Science and Engineering A342 (2003) pag 120-130.

28. G. Witz, V. Shklover, W. Steurer, S. Bachegowda, Hans-Peter Bossmann, J. Am. Ceram. Soc. 90 (9), 2935 – 2940, (2007).

ANNEX 1

Short description of IR porosimetry technique

INTRODUCTION

Recently, a potentially non-destructive technique able to estimate some APS TBC effective microstructural parameters by studying thermal diffusivity κ variations of TBC samples, when pores are filled with different gases, has been proposed [A1, A2]. In fact, thermal diffusivity/conductivity of refractory porous materials is highly sensitive to microstructural features of porosity (i.e. shape, size, orientation and overall content of pores), to porosity evolution during ageing and to the thermal properties of the gas which are dependent upon size of pores and gas pressure (Knudsen effect) [A3 - A5]. All these occurrences make in principle possible to get information, in a non destructive way, on TBC microstructure from thermal diffusivity measurements. In particular, in the case of the proposed technique, the direct model lying underneath the inversion procedure simulating the effect of microstructure on TBCs thermal diffusivity combines the Knudsen effect with the asymmetric Bruggeman model that describes the effect on the thermal conductivity of pores dispersed within a continuous ceramic matrix in terms of pore shape, orientation and content [A6]. As often highlighted in the literature, thermal diffusivity is particularly sensitive to crack-like pores with their thickness oriented parallel to the heat flux and significantly less to pores with all the other shapes and orientations. For this reason this approach does not allow a full characterisation of pores but it can give relevant information of horizontal inter-lamellar crack-like pores. Nevertheless, if additional information about intra- and inter- lamellar pores is available, the method can provide a comprehensive description of TBCs porous structure. For example, if also complementary information furnished by other techniques such as quantitative image analysis (IA) and Mercury Intrusion Porosimetry (MIP) is available to statistically analyse the orientation and thickness of the pores, a more robust estimation of effective TBC microstructure parameters can be carried out. Furthermore, if parameters estimated by merging together information supplied by all these techniques are used as input for a sintering model such as that developed few years ago by Cipitria et al [A7], a forecast of the evolution of both microstructure and thermal properties as a function of time and temperature can be obtained.

THEORETICAL REMARKS

The Bruggeman model for the thermal conductivity of a two-phase medium

To invert experimental data of thermal diffusivity to the coatings microstructure, the asymmetric Bruggeman model has been used. The thermal conductivity k of a two-phase asymmetric medium containing a volumetric fraction f of dispersed spheroids (in this case the pores) with thermal conductivity k_d, shape factor F (the depolarisation factor) and the symmetry axis parallel or vertical in respect to the heat flux can be expressed as [A6]:

$$(1-f)=\left(\frac{k_m}{k}\right)^{\varsigma}\frac{k_d-k}{k_d-k_m} \tag{A1}$$

$$\varsigma=\frac{F(1-2F)}{1-(1-F)\cos^2\alpha-2F(1-\cos^2\alpha)} \tag{A2}$$

where k_m and α are the thermal conductivity of the continuous matrix and the orientation angle between the symmetry axis and the heat flux. The more general equation valid for all the orientations can be found elsewhere [A8].

By suitably choosing the ratio of the spheroid's axes, the spheroid shape can be varied from a cylinder up to a flat lamella to match predicted and measured conductivities k. The thermal conductivity of the YPSZ matrix k_m for poly-crystals has been considered.

Since this model accounts only for a single pore shape while the porosity of APS TBC consists typically of inter-lamellar spheroidal pores and either transgranular or intergranular microcracking, a specific procedure is needed. In particular, a possible approach to extend these models to a manifold porosity

system consists of iteratively applying two-phase modelling, as explained more in detail elsewhere [A8]. It is important to note that the thermal conductivity k_d of a gas within pores decreases when the pore thickness is similar or smaller than the mean free path λ of gas molecules at pressure P and temperature T as follows [A3, A5]:

$$k_d = \frac{k_{gas}}{1 + C\left(\frac{T}{P\delta}\right)} \tag{A3}$$

where $C = \frac{4\beta(2-A)R_g}{\Pr(\beta+1)A\sqrt{2}\pi d^2 N_a}$ with $\beta = C_p/C_v$, and R_g, Pr, N_a, d *as* the ratio of the specific heats, gas constant, Prandtl number, Avogadro number, collision diameter of the gas respectively and A is an accommodation coefficient which is usually assumed to be 1 for TBC.

The fact that the thermal conductivity of each gas is differently affected by the pore size δ has been used to estimate an effective average thickness of inter-lamellar pores within TBC. The free convection within pores of TBC can be neglected being the Grashof number significantly below the threshold value of 1000.

The inversion procedure

The main objective of this approach is to find a unique solution to the inverse problem. The higher the number of pore families entered into the TBC model the higher the number of free parameters in the inversion process. The direct consequence of increasing the number of free parameters is the loss of a unique solution caused by the existence of several local minima. To avoid this problem and taking into account that the system of the n-equations referred to the n-experimental conditions is not necessarily orthogonal, the maximum number m of free parameters has to be limited (in the specific case of this work m=2). As explained below, for through thickness thermal diffusivity data, pore families can be limited to horizontal pores and globular voids with aspect ratio and pore thickness being the two free parameters.

For each sample, the inversion procedure based on the direct Bruggeman model consists in the following steps:

1. to estimate the overall content of porosity and the volumetric fractions of each pore class (i.e. inter-lamellar, intra-lamellar and globular voids) by IA; lamellar pores are divided in horizontal ($0<\alpha<\pi/6$), vertical ($\pi/3<\alpha<\pi/2$) and elsewhere oriented ($\pi/6<\alpha<\pi/3$). It is unpractical to consider angle variations, and for horizontal pores $\alpha=0$ is assumed, whereas $\alpha=\pi/2$ for vertical ones. All other pores will contribute to the thermal resistance in a complex way. To simplify the problem, the contribution of these elsewhere oriented pores are considered to be independent from each other and their effects can be considered simply by rotation of the thermal conductivity tensor. Since angular averaging gives $\left\langle (\cos\alpha)^2 \right\rangle = \frac{1}{3}$, one third of the elsewhere oriented pores is attributed to horizontal pores and the remnant part to vertical cracks. It is indeed a simplification of the procedure but it gives an effective way to characterize the coatings microstructure.

2. by using the Bruggeman model to estimate, for each experimental condition, the thermal conductivity k_{m0} of a porous TBC containing only globular voids and vertical cracks whose volumetric fractions are equal to those estimated in the previous step by IA. According to the MIP outcomes the size of globular voids for all the samples a radius of 2.75 µm has been fixed. As concerns vertical cracks spacing it has been fixed equal to $a_0=L_0=3.25$µm while crack aspect ratio and thickness have been estimated taking into account the volumetric fraction of these cracks. Typical aspect ratio and thickness values for as sprayed samples ranges between 1/50 – 1/70 and 0.1 – 0.17 µm, respectively. Although the sample to sample variation is noticeable, it gives a negligible variation in k_{m0} .

3. To estimate the thickness and the aspect ratio of horizontal pores by inverting the experimental thermal diffusivity data obtained in different environments. The estimation has to be done by fixing two parameters in the Bruggeman model for horizontal pores and using them as input within the inversion procedure: km0 (from step 2) and the volumetric fraction of horizontal pores, as estimated in the previous step by IA. In particular, in the inversion procedure, Eq.(A1) has to be solved for all the experimental conditions (i.e. gas and pressure). In the specific case of this work, the pore thickness and the aspect ratio have been estimated solving a system consisting of seven Eq.(A1) according to the seven experimental data sets obtained, In the third step of the procedure the thermal conductivity *k* of the TBC with pores filled by the different gases has been estimated from experimental thermal diffusivity values κ taking into account that:

$$k = \kappa \rho C_p$$

$$(\rho C_p)_{TBC+gas} = \rho_{gas} C_{p\,gas} f_{gas} + \rho_{TBC} C_{p\,TBC} (1 - f_{gas}) \qquad \text{(A4)}$$

To predict the evolution of thermal diffusivity as a function of sintering time and temperature, the complete set of microstructural parameters, as estimated by IA and by the inversion procedure, are translated into equivalent input parameters for the sintering model. The splat thickness $2z_s$ (typically between 1 – 6 μm) and the distances $2a$ and $2L$ between neighbour vertical cracks (typically between 4 – 10 μm) have been chosen by considering the average values measured by IA.
The evolution of the microstructural parameters, as described by the sintering model, are used as input for the Bruggeman model to estimate the thermal diffusivity evolution as a function of sintering time and temperature. Furthermore, by using the microstructural parameters describing each type of pores, an estimation of the specific surface area has been performed as the mean effective parameter to be compared to MIP experimental data.
For comparison purposes with sintering forecasts, the inversion procedure was applied to the experimental thermal diffusivity data of aged samples, as well.

REFERENCES ANNEX 1

A1. Cernuschi F., Bison P., Moscatelli A., Acta Mater 2009;57: 3460–71

A2. F. Cernuschi, I.O. Golosnoy, P. Bison, A. Moscatelli, R. Vassen, H.-P. Bossmann, S. Capelli, Acta Mater 2013;61: 248–62

A3. Mc Pherson R., Thin Solid Films, 1984; 112: 89 – 95.

A4. Litovsky E. Ya, Shapiro M., J. Am. Ceram. Soc., 1992; 75 (12): 3425-39.

A5. M. Knudsen, The kinetic theory of gases, 3rd ed., Wiley, New York, 1950.

A6. D. A. G.Bruggeman, Ann. Physik, 1935;24: 636-64.

A7. Cipitria A., Golosnoy I.O., Clyne T.W., Acta Mater. 2009; 57: 980 –92.

A8. Cernuschi F., Ahmaniemi S., Vouristo P., Mäntylä T. J. European Ceram. Soc. 2004; 24: 2657-67.

A9. Cipitria A., Golosnoy I.O., Clyne T.W., Acta Mater. 2009; 57: 980 –92.